Size and geometry of microearthquake seismic ruptures from *P* and *S* pulse width data

Salvatore de Lorenzo[1] and Aldo Zollo[2]

[1]*Dipto. di Geologia e Geofisica, Università di Bari, Campus Universitario, Via Orabona* 4, 70125 *Bari, Italy. E-mail: delorenzo@geo.uniba.it*
[2]*Dipto. di Scienze Fisiche, Università di Napoli, Naples, Italy*

SUMMARY

We propose a method to estimate the radius, dip and strike of a circular seismic rupture through the inversion of first *P*- and *S*-wave pulse widths measured on microearthquake records.

The method is based on quite general, numerically calibrated relationships relating source and *Q* parameters under the assumption that the waves are radiated by a circular crack propagating at a constant rupture velocity.

To study the influence of both the source and receiver configuration and the properties of seismic rupture, a detailed resolution study on synthetic data has been carried out. For a microearthquake rupture, the pulse width variations with azimuths depend critically on the fault plane orientation and the resolution on fault angle parameters can be qualitatively assessed by the parameter η, defined as the relative variation of the take-off angles with respect to their average value. A statistical approach based on mapping random deviations on data in the (δ, ϕ) parameter space has been adopted to quantify the uncertainty affecting the fault plane estimates. The method is applied to estimate the source parameters of an $ML = 3.1$ event recorded during the 1997 Umbria-Marche earthquake sequence.

For the considered event, the fault plane solution is in good agreement with the $\delta-\phi$ estimates obtained by the method of the joint inversion of *P* polarities and *S* polarizations.

Key words: directivity, fault plane orientation, multipathing, pulse width.

1 INTRODUCTION

In the recent past, many efforts have been made in an attempt to detail seismic source properties of low and moderate earthquakes by the study of the recorded waveforms (Mori & Hartzell 1990; Mori 1996; Deichmann 1997, 1999). This can become a complex problem since the source and propagation parameters (fault dimension, rupture velocity, quality factor) can trade-off on seismograms, in the frequency and/or the time domain (Scherbaum 1990; Deichmann 1997).

Concerning the amplitude and shape of first *P*- and *S*-wave arrivals, the dominant propagation effects are the geometrical spreading and the anelastic attenuation. Generally, homogeneous or vertically varying elastic media are assumed to evaluate the geometrical amplitude decay with distance. Instead, the anelastic effect of the Earth is accounted by the *P* and *S* quality factors, controlling the exponential decay of the amplitude spectrum and the pulse broadening with the travel distance and frequency. Several *Q* studies have shown that, as a consequence of the heterogeneity of the crust and site effects, *Q* can suffer significant lateral and vertical variations and these result in differential variations of the shape of the waves

recorded at different sites, thus increasing the complexity of the problem.

On the other hand, the seismic moment, the radiation pattern and the rupture directivity are the main source effect. Then the effect of the seismic source may also be more complex, since the shape of the recorded waves is a function of several source parameters such as the fault dimensions, the rupture velocity and the fault plane orientation.

At least three general different approaches to the joint modelling of source parameters of low magnitude earthquakes and *Q* have been proposed over the last 20 years.

The most used techniques are the spectral methods (see, e.g. Abercrombie 1995); these consist of assuming that the far-field source spectra can be described through a circular crack model (Brune 1970; Boatwright 1980), which predicts a flat spectrum below the corner frequency f_0 and decaying as an inverse power of the frequency (with a source-model-dependent exponent) above f_0; the effect of attenuation on seismic spectra is modelled as an exponential decreasing function of the ratio $2\pi f t/Q$, where t is the traveltime and f is the frequency. This approach, first proposed by Anderson & Hough (1984), has been largely adopted (e.g. Scherbaum 1990;

Ichinose *et al.* 1997; Hough *et al.* 1999). Since the technique is based on an isotropic source model it is not required to invert for the fault orientation and this allows for a reduction of the number of parameters (the corner frequency and the high-frequency fall-off exponent) to be inferred.

Another approach to the study of the seismic source properties for moderate ($M > 4$) and great earthquakes is based on the use of the empirical Green function (EGF) (Zollo *et al.* 1995; Courboulex *et al.* 1996; Abercrombie *et al.* 2001). The EGF technique consists of extracting directly from the data an empirical function F selected in such a way as to be representative only of instrument and path effects (Hartzell 1978); after the deconvolution of the other waveforms with F a representation of the source far field is achieved.

Finally, in the time domain, the most used technique is represented by the rise time or pulse width method (Gladwin & Stacey 1974; Wu & Lees 1996). Deichmann (1999) showed that the methods based on pulse widths tend to better estimate seismic source parameters compared with the EGF technique, since the spectral ratio operated in the EGF deconvolution process tends to produce noise magnification that could mask the initial onset of the considered wave, in particular when this is slow. Wu & Lees (1996) showed that the linear relationships on which the rise time method is based still remain valid if we consider a finite-dimension isotropic seismic source characterized by a frequency cut-off at the source greater than or equal to 20 Hz, also if the slope of the pulse width versus t^* is source dependent. Nevertheless, experimental results (Blair & Spathis 1982) and theoretical analyses (Liu 1988; de Lorenzo 1998) indicated that the linearity on which the method is based is only apparent, in that the slope of the straight line describing pulse width versus traveltime is a function of the source frequency content.

Since the source frequency content is different at different sites, as a consequence of the finiteness of the rupture velocity and the source dimensions (Sato & Hirasawa 1973; Madariaga 1976) in some cases the plots of pulse width versus distance do not exhibit a clear increasing trend; in particular, this could happen if the medium is not strongly attenuating and/or the epicentre of the event lies inside the area enclosed by the acquisition network, so that the attenuation term is almost the same at different stations. In these cases the duration of signals may be more sensitive to directivity variations than to attenuation. Based on these grounds, Zollo & de Lorenzo (2001) (hereafter referred to as Z&D) modified the pulse width method to account for these effects; they calibrated, for a fixed value of V_p velocity at the source, the numerical equations representing the dependence of rise time and pulse width of first P arrivals as a function of source parameters (fault radius, dip and strike of the fault plane) and Q_p; through a resolution study on synthetic data sets, based on the sources and receivers geometry of the Campi Flegrei 1984 microearthquake sequence, they showed that source dimensions and Q_p can be adequately recovered, whereas dip (δ) and strike (ϕ) estimates are usually less reliable.

In this article the Z&D method has been generalized to account for different values of V_p and V_s at the source; this allows for the application of the method to different areas and/or to different hypocentral depth ranges. In the previous study, based on the acquisition layout of the Campi Flegrei 1984 swarm, it has been shown that the limited number of only P pulses can lead to a loss of resolution on the fault plane estimates. Starting from this observation, in this article we focus more closely on the properties of the relative geometry of source and receivers and on the joint use of P and S pulse width data that are required to infer reliable estimates of the fault plane orientation.

The method has been applied to a low-magnitude earthquake ($M_l = 3.1$) of the Umbria-Marche seismic sequence (central Italy) that occurred in the period 1997 September–October. The results have been compared with those obtained by inverting P polarities and S polarizations according to the method of Zollo & Bernard (1991).

2 THE GENERAL RELATIONSHIPS BETWEEN PULSE WIDTHS, SOURCE PARAMETERS AND Q

On a velocity seismogram, the pulse width ΔT of a seismic phase can be defined as the time interval between the arrival time of the signal and its second zero crossing time (Fig. 1). If we consider the signal radiated by a point-like and impulsive source time function (a Dirac delta function) and recorded at an assigned distance, ΔT is a linear function of the attenuation term $t^* = T/Q$ that accounts for the propagation effects, where T is the traveltime of the wave and Q is the constant quality factor of the medium (Kjartansson 1979).

Let us now consider the wavefield radiated by a finite-dimension seismic source, and assume that this is due to a circular crack rupturing at a constant velocity. In the far-field range (Fraunhofer approximation), the source pulse width (i.e. the pulse width of the signal in the absence of attenuation) is given by (Aki & Richards 1980)

$$\Delta T_0 = \frac{L}{V_r} + \frac{L}{c} \sin\theta. \tag{1}$$

In eq. (1) L is the final radius of the crack, V_r is the average rupture velocity, c is the phase velocity at the source and θ is the take-off angle (i.e. the angle formed by the ray leaving the source with the normal to the fault plane). By considering the propagation in an attenuating medium of a phase radiated by a finite-dimension seismic source, the relationship that accounts for both source and propagation effects can be written as (Gladwin & Stacey 1974)

$$\Delta T = \Delta T_0 + C \frac{T}{Q}. \tag{2}$$

As we discussed in the previous section, C depends on the source frequency content; this makes the problem of retrieving Q and source parameters by inverting the pulse width data complex, since we need to assume a source model. Z&D determined C by considering the source and receiver geometry of low-magnitude earthquakes recorded during the period 1984 January–July at the Campi Flegrei caldera, by fixing the body wave velocity at the source; the circular crack model of Sato & Hirasawa (1973) was adopted as the source model, and the Azimi attenuation operator (Azimi *et al.* 1968) was assumed to account for the anelastic attenuation of rocks.
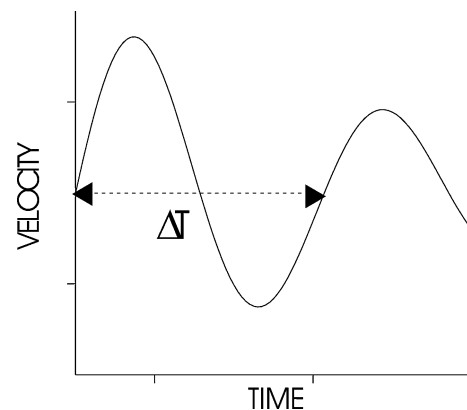

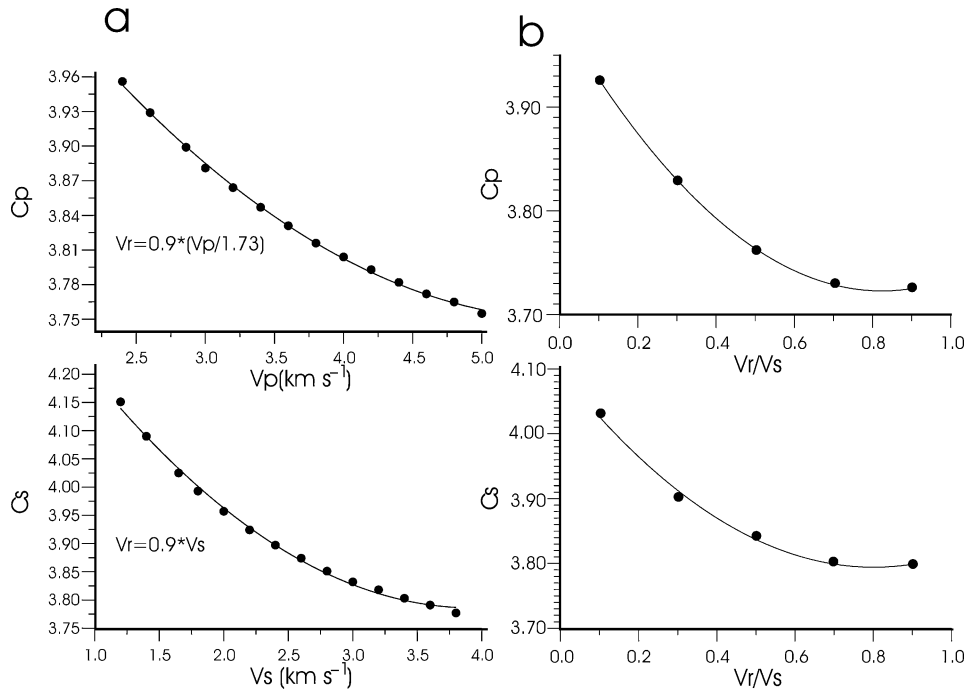**Figure 1.** The pulse widths on a velocity seismogram.

Figure 2. (a) The slope C of ΔT versus t^* for P and S waves as a function of V_p and V_s ($V_r = 0.9V_s$), (b) the slope C of ΔT versus t^* for P and S waves as a function of V_r, for $V_p = 6.1$ km s^{-1} and $V_s = 3.5$ km s^{-1} (see the text). Each dot in the figure has been computed through a regression analysis of synthetic ΔT versus t^* measured over 960 synthetic seismograms.

In order to obtain a more general formulation of the Z&D method for crustal ranges of the body wave velocities, one must evaluate the dependence of the slope C_p of the P pulse width versus t^* as a function of V_p velocity (at a given rupture velocity) and also the slope C_s of the S pulse width versus t^* as a function of V_s velocity (at a given rupture velocity). To this end, we have applied the numerical technique described in Z&D to compute C for different values of the body wave velocity at the source and of the rupture velocity. This procedure has been repeated for each of the V_p and V_s values shown in Fig. 2(a) and for each of the V_r values in Fig. 2(b).

The results of our calculation can be summarized in the following way.

(1) For a given V_r/V_s ratio C_p and C_s decrease with increasing of V_p and V_s, respectively.

(2) The dependence of C_p and C_s coefficients as a function of V_p and V_s, respectively (for the cases $V_p/V_s = 1.73$ and $V_r/V_s = 0.9$) is shown in Fig. 2(a). The least-squares fit to the results led us to the following relationships:

$$C_P(V_R = 0.9V_S) = 4.362 - 0.216V_P + 0.019V_P^2 \qquad (3)$$

$$C_S(V_R = 0.9V_S) = 4.518 - 0.372V_S + 0.047V_S^2. \qquad (4)$$

(3) At a fixed V_p (or V_s) C_p (or C_s) decreases with increasing V_r/V_s ratio.

(4) The C_p and C_s coefficients versus the rupture velocity (for the case $V_p = 6.1$, $V_s = 3.5$ km s^{-1}) are plotted in Fig. 2(b). The results of our calculation led to the following regression equations:

$$C_P(V_P = 6.1\,\text{km s}^{-1}) = 3.986 - 0.640V_R + 0.389V_R^2 \qquad (5)$$

$$C_S(V_S = 3.5\,\text{km s}^{-1}) = 4.097 - 0.755V_R + 0.471V_R^2. \qquad (6)$$

As we will detail in the next section, it is very difficult to jointly infer the source radius and the rupture velocity by inverting pulse width data of low-magnitude earthquakes. For this reason we think

that a further extension of the relations (5) and (6) to other V_p and V_s values is useless.

Details of the non-linear inversion technique for inferring model parameters, based on the simplex downhill method (Nelder & Mead 1965) are given in Z&D.

3 STUDY OF THE UNCERTAINTIES ON MODEL PARAMETERS

In this section we present a detailed resolution study based on inversions of synthetic data sets, aimed at assessing the accuracy of the model parameter estimates. In particular, we are interested in quantifying the dependence of the fault plane resolution both on the source properties and on the geometry of the acquisition network.

In what follows, we consider the source–receiver geometry of a seismic event that occurred during the 1997 Umbria-Marche (Italy) seismic sequence, which started on 1997 September 26. The temporary network deployed in the area consisted of 15 stations and detected approximately 200 earthquakes with local magnitude greater than 2.5(Fig. 3). The field acquisition was supported by the 'Gruppo Nazionale per la Difesa dai Terremoti' (GNDT, National Group for the Defense against Earthquakes) and Servizio Sismico Nazionale (SSN, National Seismic Service). Accurate hypocentral locations were obtained by combining the temporary network data with those recorded by the nearby stations of the local permanent networks (i.e. the three RSM stations managed by the Osservatorio Geofisica Sperimentale di Macerata, and the five RESIL stations managed by the 'Regione Umbria—Oss. Bina di Perugia') (Fig. 3). These data, together with the hypocentral locations, were arranged for non-profit research purposes with electronic support by Govoni *et al.* (1999).

For the considered event, 11 P pulse widths and five S pulse widths have been selected, as we will discuss in the next section. The acquisition layout and the epicentre of the event are shown in Fig. 3.
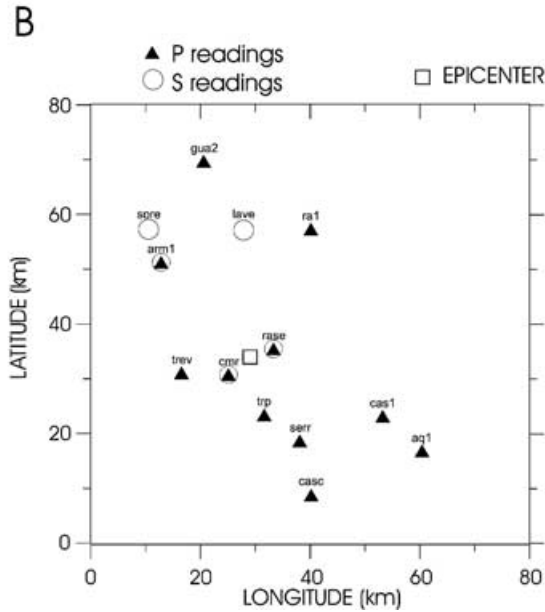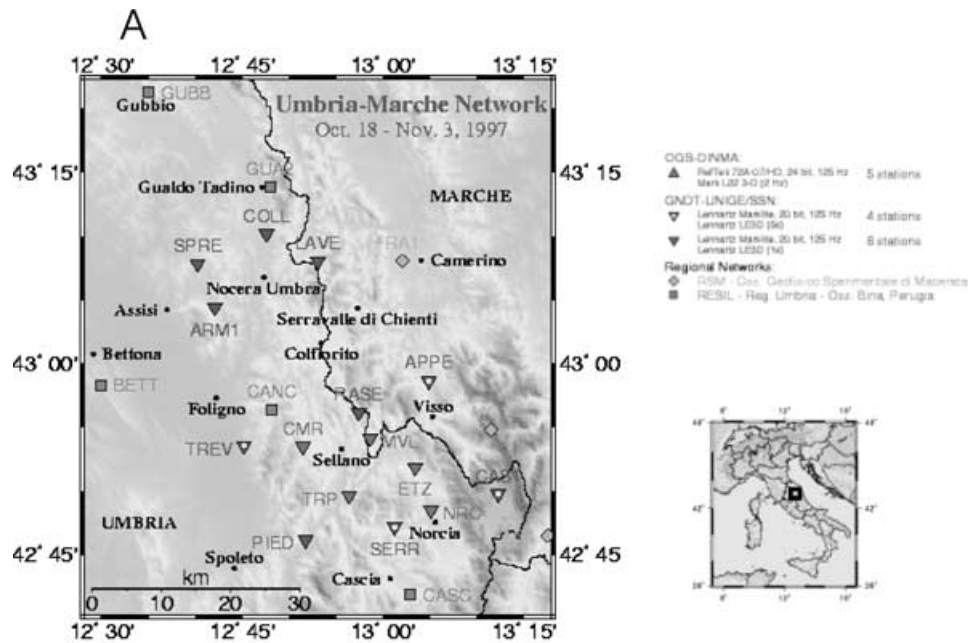
Figure 3. The source–receivers configuration of the low-magnitude earthquake ($M_l = 3.1$) considered in this study. (a) The complete (temporary + permanent) array deployed in the Umbria-Marche (central Italy) region (modified by Govoni *et al.* 1999). (b) The stations considered in this study for which *P* and *S* pulse widths are available. Triangles refers to *P* pulse widths and circles to *S* pulse widths.

The following parameters have been assumed: $V_p = 6.1$ km s^{-1}, $V_s = V_p/1.9$ (Cattaneo *et al.* 2000) and $V_r = 0.9 V_s$.

In order to study the fault plane resolution the following procedure has been used.

(1) First of all, synthetic noise-free *P* and *S* pulse widths have been computed through the above calibrated equations, by fixing the model parameters. To simulate the effect of noise on data we used the random deviations technique (Vasco *et al.* 1995). Each synthetic data set has then been modified, by adding to each data a random quantity selected in the range of a given uncertainty (we assumed a percentage error of 5 per cent for both *P* and *S* waves).

This procedure has been repeated 50 times in order to obtain 50 independent data sets. These have then been inverted in order to obtain 50 estimates of each model parameter and the best-fitting model parameters $m_{est} = (L, \delta, \phi, Q_p, Q_s)$ have been retrieved from the statistical analysis of the results.

(2) Secondly, we fixed L, Q_p and Q_s at the values inferred by the inversion and computed the variations of the standard deviation σ among data and their estimates with varying dip and strike of the fault. The σ values were computed on a dense grid (5 × 5 deg^2) in the δ–ϕ plane. The standard deviation was normalized to the average residual σ_0 on pulse widths, this last being computed by the relation $\sigma_0 = \frac{1}{N} \sum_{i=1}^{N} |0.05 \Delta T_{obs}^i|$. The σ/σ_0 plot in the (δ, ϕ)
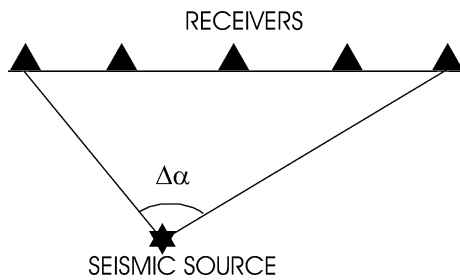
RECEIVERS

Figure 4. The angular range $\Delta\alpha$ for a given source–receivers configuration. It represents the angle at which an observer located at the source views the array.

plane allows us to obtain an immediate graphical representation of the fault plane resolution. In fact, a well-resolved solution will be generally represented by a σ/σ_0 function sharply peaked, or bell-shaped, around the best-fitting solution, whereas a poorly resolved solution will correspond to a σ/σ function more widened around the best-fitting value and/or presenting secondary minima. By plotting the σ/σ_0 function in the (δ, ϕ) plane, a simple quantitative estimate of uncertainty of the inferred (δ, ϕ) solution is obtained by the length of the semi-axes of the ellipse, in the (δ, ϕ) plane, that encloses the points having $\sigma/\sigma_0 < 1$.

The first point we address is the sensitivity of the inferred solutions to variations of the angular range of the source–receiver layout. We indicate with $\Delta\alpha$ the angle formed by the straight lines connecting the hypocentre with the two furthest receivers (Fig. 4). This angle represents the angular coverage of the source–receiver configuration and progressively decreases with increasing source depth. It does not depend on the source orientation. We can *a priori* expect that the accuracy of the fault plane estimates will depend on both $\Delta\alpha$ and on the number of available data.

In Figs 5(a) and (b) the plots of the $\sigma(\delta, \phi)/\sigma_0$ function, arising from two different true fault plane orientations, for different values of $\Delta\alpha$, are shown. In both cases the resolution tends to increase with increasing of $\Delta\alpha$ (i.e. with decreasing depth of hypocentre). For the two examples given in Figs 5(a) and (b) the resolution is an increasing function of $\Delta\alpha$ (the best result is for $\Delta\alpha = 124°$, equivalent to a hypocentre located at 10 km depth). Only at great depths ($z = 80$ km) does the shape of the σ/σ_0 function tend to strongly widen in the strike direction (the uncertainty on strike is equal to $\pm20°$ for an event having a hypocentral depth equal to 80 km, as inferred from both Figs 5a and b). These results indicate that the Umbria-Marche array should be very suitable for studying the source properties of the 1997 Umbria-Marche sequence, the foci of which have been localized between approximately 0.6 and 10 km (Govoni *et al.* 1999).

However, results of Fig. 5(a) ($\delta = 45°$, $\phi = 300°$) are better than those of Fig. 5(b) ($\delta_{\text{true}} = 30°$, $\phi_{\text{true}} = 90°$). This is mainly a consequence of the directivity effects, which increase with increasing source radius ($L = 200$ m in Fig. 5a, $L = 100$ m in Fig. 5b).

We point out that, with increasing depth of the earthquake focus the P- and/or S-wave amplitudes could become comparable with the noise level, producing a lowering of picking quality. To study this effect would require another approach to the simulation of noise (based on calculation of noisy synthetic seismograms) not used here.

The second point we have studied is the sensitivity of the inferred fault-plane solutions to the variations of the radius L of the seismic source. It is clear (eq. 1) that, given the orientation of the fault plane

and the attenuation structure of the medium, the variations of ΔT with respect to their average value decrease with decreasing crack dimension. What is the minimum radius at which the fault plane is still detectable? We studied this problem, for different fault plane angles and quality factors of the medium. In Figs 6(a) and (b) two different tests are shown; in both the examples a progressive sharpening of the σ/σ_0 function around the best-fitting solution, with increasing fault radius, can be deduced; results of Fig. 6(a) indicate that the fault plane resolution is very small for $L \leq 30$ m, whereas results of Fig. 6(b) indicate a minimum source radius $L = 10$ m; this indicates that the minimum fault radius which allows the detection of the fault plane depends on the seismic source orientation. The reason for this will be clear from the next two examples.

The other questions that need to be addressed are the following: how much does the inferred fault plane solution depend on the true fault plane orientation? Are there preferable orientations for which the solutions are better constrained by the inversion? Are there dip and strike ranges for which we can *a priori* estimate an unacceptable loss of resolution? Is it possible to define a parameter that describes this '*a priori*' information?

In order to answer these questions we have carried out two types of synthetic tests: in the first, we have fixed all model parameters, with the exception of the fault dip δ, and have analysed the variations of the shape of the σ/σ_0 function with varying δ (Figs 7a and b); in the second we have fixed all model parameters, except the fault strike ϕ, and have analysed the σ/σ_0 variations with varying ϕ (Figs 8a and b). The simulations shown in Fig. 7(b) ($\phi = 50°$) indicate that resolution tends to reach its maximum when δ is around $70°$, with an uncertainty on dip and strike of only $\pm2°$; for $\delta < 15°$ the σ function tends to broaden along the strike direction (resulting in an uncertainty on strike equal to $\pm20°$), even if the solution is sufficiently recovered. In contrast, when $\delta > 85°$ secondary localized minima appear. It is worthwhile to note that in all the simulations performed, the two different solutions retrieved for $\delta > 85°$ are always around $\phi = \phi^{\text{true}}$ and $\phi = \phi^{\text{true}} + 180°$. This effect is simply explained by remembering that at $\delta = 90°$ the strike angle is defined at less than $180°$. Therefore, this secondary solution does not result in a critical ambiguity, in that, for $\delta = 90°$, the two fault planes represent the same fault and not the true and the auxiliary fault plane as inferred by P polarities.

We found that the fault plane resolution is well related to the values assumed by the η parameter, defined as

$$\eta = \frac{\Delta\theta}{\theta_{\text{ave}}} = \frac{|\theta_{\text{max}} - \theta_{\text{min}}|}{\theta_{\text{ave}}}, \tag{7}$$

where θ_{max}, θ_{min} and θ_{ave} represent the maximum, minimum and the average value of the takeoff angle, respectively; η represents the relative variation of the takeoff angles with respect to their average value. Clearly, given the source–receivers geometry and the source radius, the η variations are only due to the different orientations of the fault plane. The reliability of the fault plane solution increases with increasing η. This result is confirmed by the tests shown in Fig. 7(a) (strike equal to $150°$). In this case the maximum value of η is for $\delta = 80°$, which also corresponds to the best shape of the σ function.

The striking correlation among resolution and η is better described in the examples shown in Fig. 8 (δ is fixed and ϕ varies). In particular (Fig. 8a), the worst result is for $\phi = 180°$, which corresponds to the lower η. In Fig. 8(b) ($\delta = 60°$) the better result is obtained for $\phi = 300°$, which corresponds to the highest η, whereas the maximum uncertainty (approximately $\pm8°$ on dip) is found at the lowest η ($\eta = 0.86$, $\phi = 220°$).
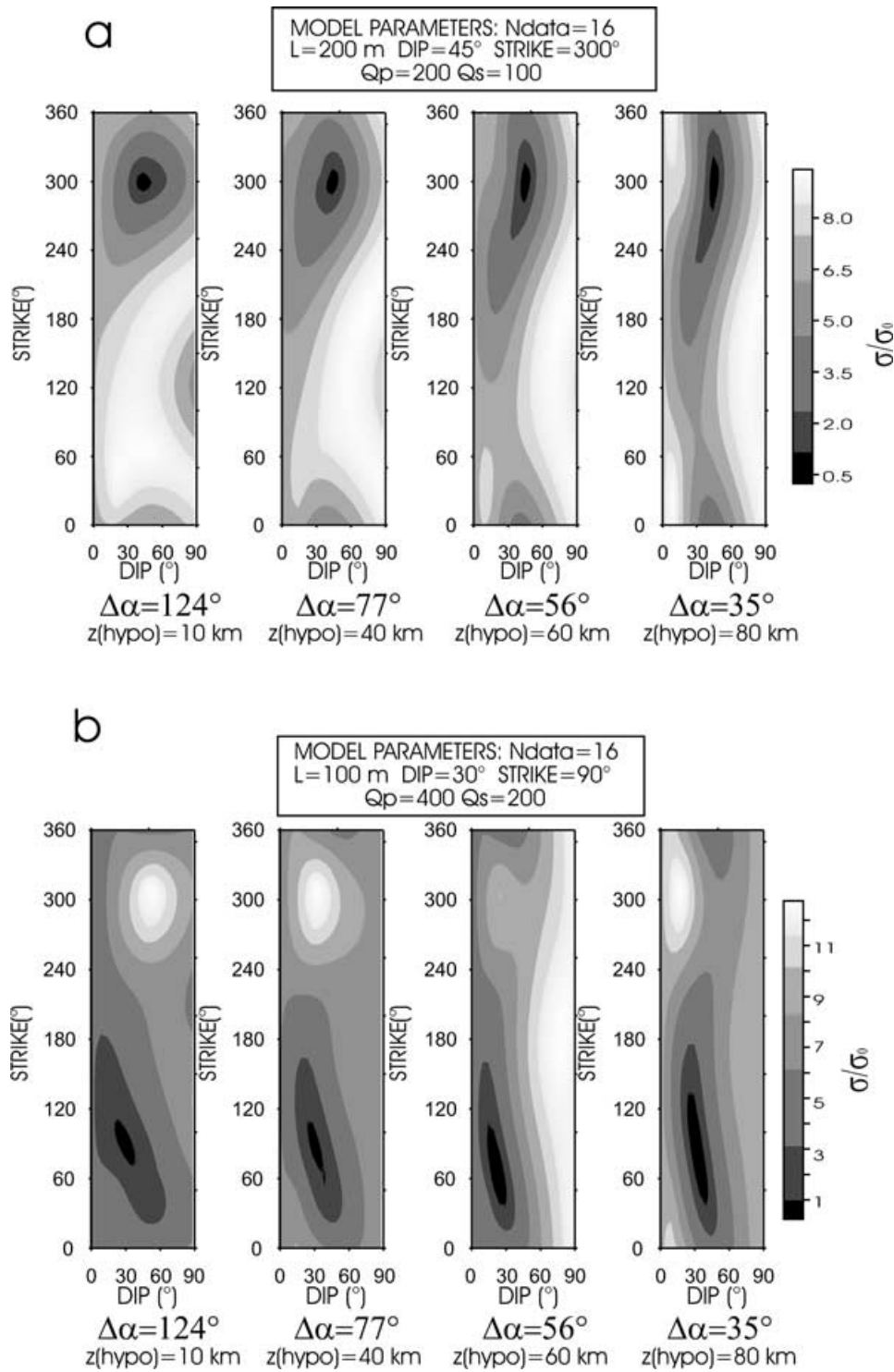
Figure 5. (a), (b) Study of the fault plane resolution as a function of the angular range $\Delta\alpha$: plot of the $\sigma(\delta, \phi)/\sigma_0$ function in (δ, ϕ) space. On the bottom of each figure are reported the angular range $\Delta\alpha$ and the hypocentral depth used in the simulation.

In Fig. 9 the distribution of the η parameter in the (δ, ϕ) plane for the considered source–receivers geometry (source depth to 3.7 km) is represented, together with the theoretical source pulse widths corresponding to a low and a high η; it is worthwhile to observe that regions in the (δ, ϕ) plane with low η are associated with small variations of the source pulse widths due to a reduction of directivity variations, whereas (δ, ϕ) areas having a high η are related to higher variations of the source pulse widths due to the enhancing of directivity effects. Therefore, the representation of the η parameter in the δ–ϕ plane gives *a priori* useful insights into the fault plane
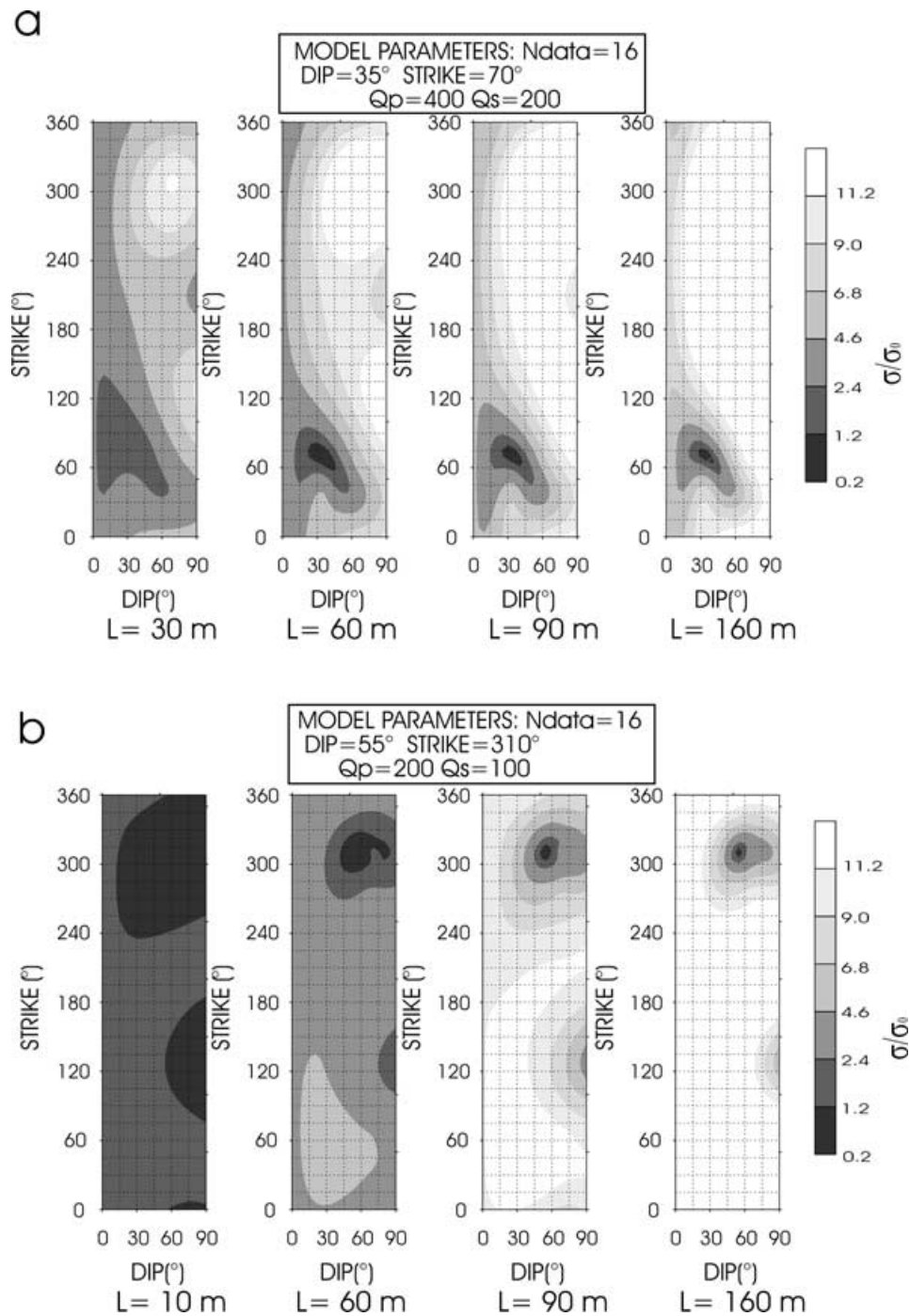
Figure 6. (a), (b) Study of the fault plane resolution as a function of the source radius: plot of the $\sigma(\delta, \phi)/\sigma_0$ function in (δ, ϕ) space. On the bottom of each figure is reported the source radius used in the simulation.

resolution, in that low η will be related with *a priori* poorly resolved fault planes and high η will be associated with well-resolved fault planes.

4 EXAMPLE OF APPLICATION

In this section we present the application of the method to the study of the fault plane orientation of a microearthquake that occurred in the Umbria-Marche region in 1997; the event has been recorded at 21 stations of the above described temporary array located in the area during the earthquake crisis. 11 *P* pulse widths and five *S* pulse widths have been selected by the waveforms analysis, as we will detail in the next section. The earthquake hypocentre was located at a depth of 3.7 km (Govoni *et al.* 1999) and the source–receiver configuration (Fig. 3) coincides with that considered in the above resolution analysis (Figs 6–9).

4.1 Pulse width measurements

The velocity seismograms have been corrected for the instrumental responses given in Govoni *et al.* (1999). Fig. 10(a) shows the vertical component of the considered traces. Owing to the generally higher
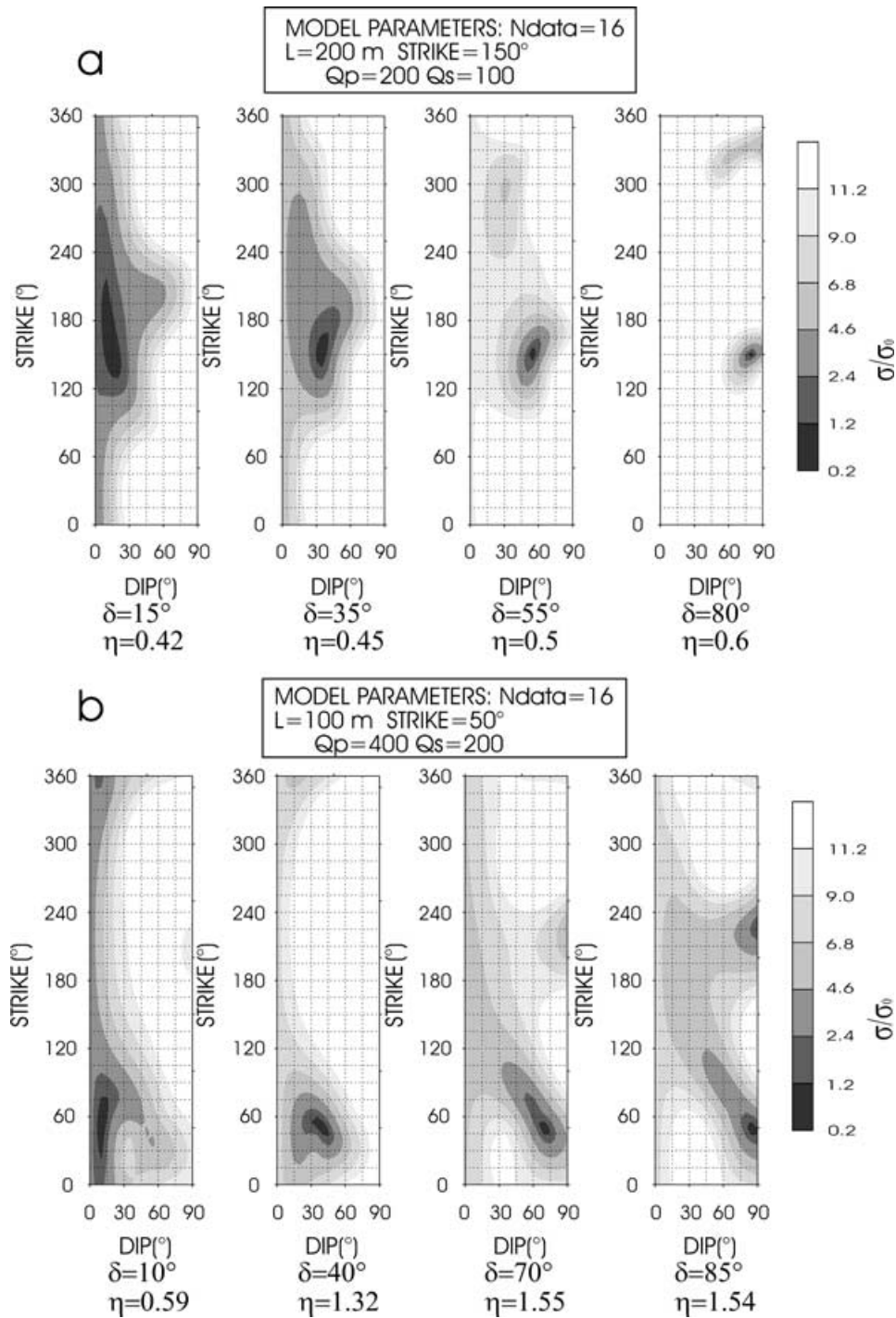
Figure 7. (a), (b) Study of the fault plane resolution as a function of the fault dip: plot of the $\sigma(\delta, \phi)/\sigma_0$ function in (δ, ϕ) space. On the bottom of each figure is reported the theoretical dip used in the simulation and the value of the η parameter (see the text).

amplitude of the vertical component of the first motion, the *P* pulse widths have been measured on this component.

A detailed study has been carried out to evaluate whether site effects and/or source complexity can alter the shape of the *P* pulse, introducing a bias in the pulse width measurements.

The site effects are often recognized as being the cause of the secondary arrivals after the first *P* motion. These arrivals are usually attributed to the presence of thin layers around the recording site,

in which part of the wavefield remains trapped and is subject to multiple reflections. When these secondary waves arrive after the first period of the *P* motion, the source time function of the event is preserved and can be used to model the source process (fig. 5 of Deichmann 1999). In other cases, multipath effects produces a discontinuity in the observed first *P* pulse shape, which is easily inferred from a visual inspection of seismograms (Liu *et al.* 1994; Deichmann 1999; Courboulex *et al.* 1999, among the others). In our
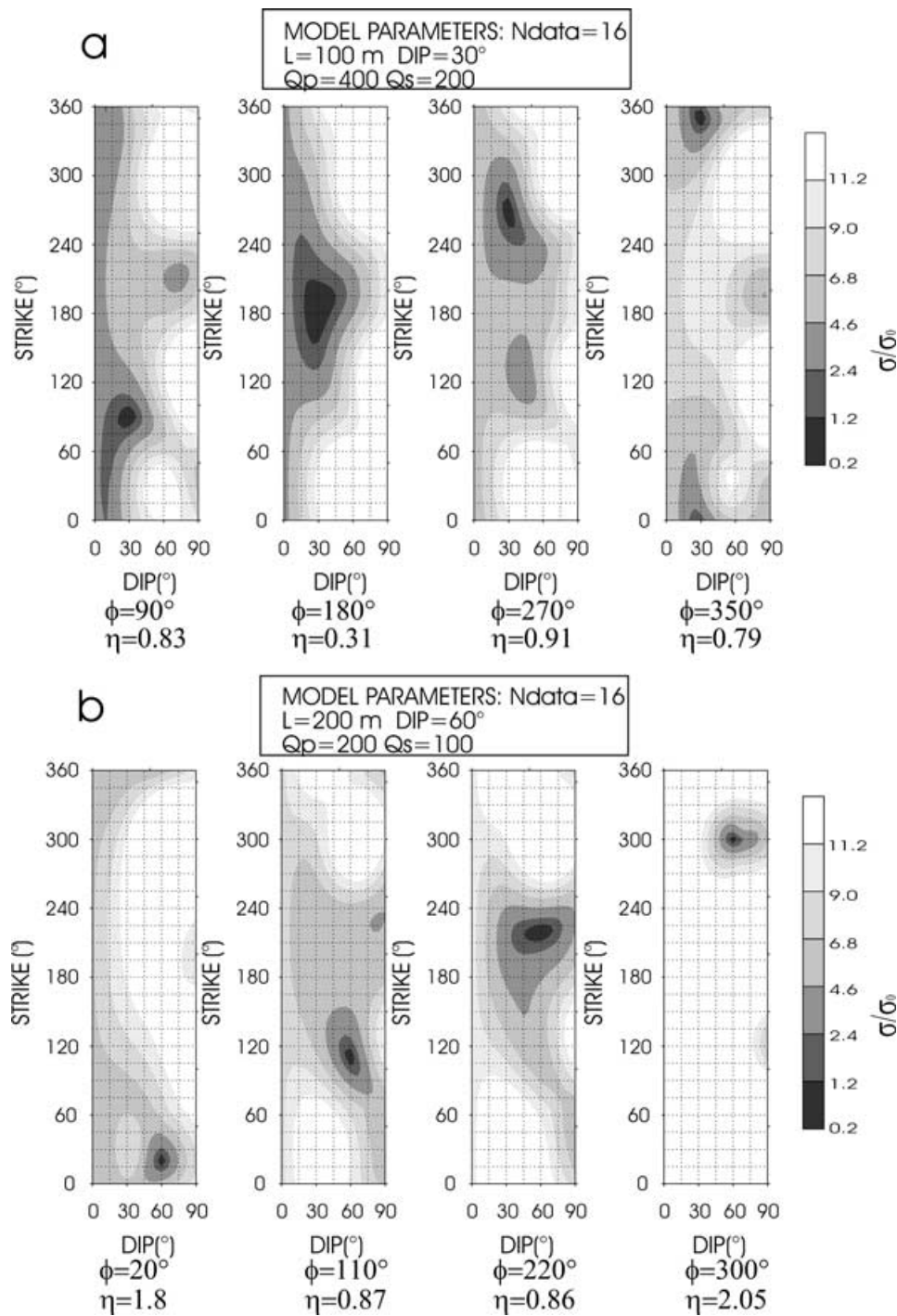
Figure 8. (a), (b) Study of the fault plane resolution as a function of the fault strike: plot of the $\sigma(\delta, \phi)/\sigma_0$ function in (δ, ϕ) space. On the bottom of each figure is reported the theoretical strike used in the simulation and the value of the η parameter (see the text).

work, the recorded *P*-wave pulses with a clear discontinuity during the first period of *P* motion have been discarded. Some of these are shown in Fig. 10(b).

The remaining traces do not show multiple arrivals during the first period of *P* motion and have been used in the study of the fault plane orientation.

Concerning the possible effect of source complexity, we analysed the *P*-wave displacement waveforms. With the exception of the station RASE, the first *P* displacement waveforms closely match the

simple unipolar shape expected from the S&H theoretical source model (Fig. 10c).

It is worthwhile to observe that a time difference between the time duration as measured on velocity traces and the same as computed on displacement traces is inferred (Table 1). These differences may be attributed either to source complexity (e.g. Boatwright 1984) or to a residual interference with the *P* coda; they also indicate the resolution on *P* pulses and have been used to estimate the average uncertainty on our measurements (9 per cent), as reported in Table 1.
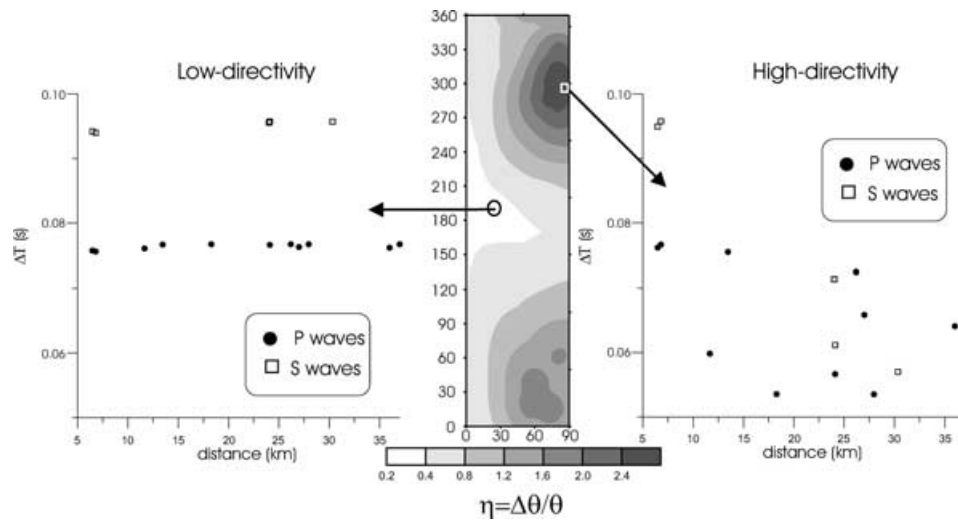
Figure 9. The effect of directivity variations with variation of the true fault plane orientation; the map at the centre of the figure gives the η distribution in (δ, ϕ) space. On the left is shown the plot of pulse widths versus distances for a low-η fault, defined by the circle in the η map. On the right is shown the plot of pulse widths versus distance for a high-η fault, defined by the square in the η map.

Table 1. *P* pulse width estimation.

Station	Pulse width on velocity seismogram (s)	Pulse width on displacement seismogram (s)	Percentage difference
AQ1	0.148	0.150	1.4
RA1	0.193	0.171	11
GUA2	0.218	0.186	19
CASC	0.156	0.143	8
ARM1	0.146	0.125	13
RASE	0.138	0.121	12
CMR	0.123	0.133	8
TRP	0.176	0.166	5
SERR	0.122	0.119	2
TREV	0.127	0.129	1.5
CAS1	0.148	0.173	17
			Average = 9

We used as a *P* pulse width the average value between the ΔT estimated on the velocity seismogram and the same as measured on integrated displacement traces (Fig. 10c), and assumed that the uncertainty associated to the *P* pulse width is the semi-difference of these two values.

The estimation of the *S* pulse width is more difficult to obtain, owing to the interference of the *S* phase with the signals following the *P* phase, usually generated around the recording site. These secondary arrivals tend to reduce the quality of the *S* phases, making the uncertainty on the *S* pulse widths more difficult to evaluate. Bandpass filtering of the traces could certainly help to reduce the contributions of the high-frequency phases generated around the recording site, but may severely bias the duration of the signals (in particular, the smoothing of the ascending part of the signal caused by filtering could produce a shift of its time onset and broaden the waveform), so that we choose to work on unfiltered traces. Moreover, for these reasons, only a limited number (five) of *S* pulse widths have been extracted from the analysis of the complete data set. In the analysis of *S* pulse widths we essentially followed the outline first given in Bernard & Zollo (1989). After a thorough study of the complete wavefield generated by a double-couple source, the authors inferred that some useful criteria should be satisfied in order to use

the *S*-wave waveforms for source studies. Based on a parametric study on complete waveform synthetics, they concluded that the stability with time of the *S* polarization and the dominance of the horizontal motion are good criteria for selecting *S* waveforms to be used for source parameter investigation.

When data are far from these criteria there may be several causes. In the near-source range the most frequent are the generation of a local *SP* phase caused by coupling at a free surface of incident *SV* with reflected *P* and *SV* near the critical angle, or generation of other multiples (Bernard & Zollo 1989) or the presence of an anisotropic elastic layer, beneath the recording site, which causes the widely observed phenomenon of *S*-wave splitting (Crampin 1985; Zollo & Bernard 1989; Huang *et al.* 2000).

A complete analysis of *S*-wave polarization has been performed in order to test the polarization stability with time. According to the above-mentioned criteria, we discarded all *S* waves characterized by the dominance of a vertical component, which may indicate an important contribution of near-site *S-to-P* converted arrival on the *S* waveform.

For the remaining traces, the analysis of the particle motion in the *S*-wave window shows that, the *S* signal is mainly polarized along a single direction, which is related to the source mechanism and location (Fig. 11a).

According to the polarization analysis, the measurements of *S* pulse width have been performed on the record that has been obtained by rotating the N and E component along the dominant *S*-wave polarization direction (hereinafter referred to as the R direction) (Fig. 11b). The estimated *S* pulse widths are shown in Fig. 12.

However, the quality of *S* pulse widths cannot be compared with that of *P* phases. In fact, even if our procedure tends to minimize the role of secondary arrivals on the R component, it is not able to completely remove them. To better pick the onset of *S* phase, we then compared the *S* waves with the squared traces (Fig. 12), as suggested by Boatwright (1980) and computed the difference between the *S* pulse width as measured on the velocity seismogram and the same as measured on the squared trace, as shown in Fig. 12 and reported in Table 2. At station SPRE the onset of the phase has been chosen also taking into account the particle motion of Fig. 11(c), from which
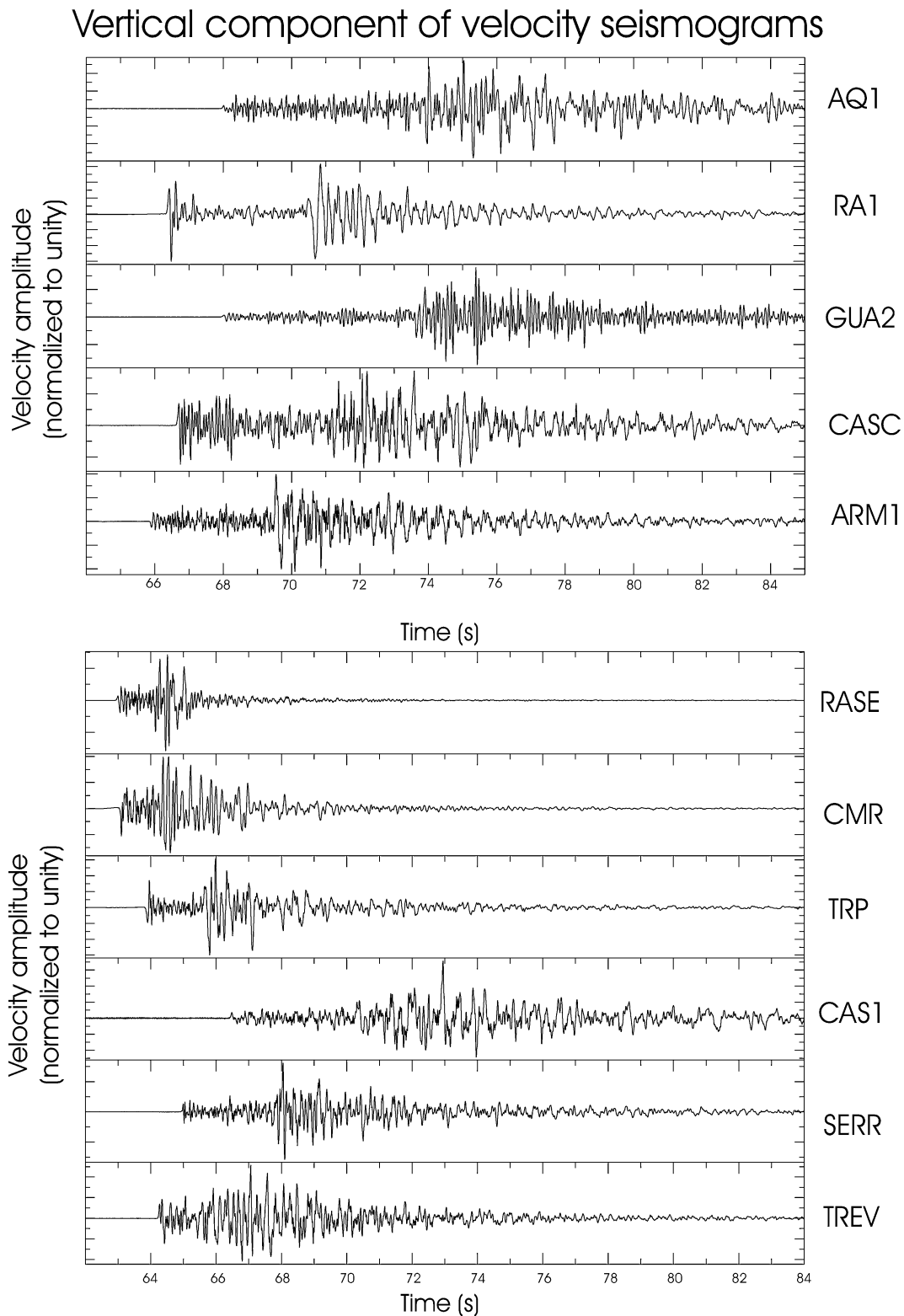
Vertical component of velocity seismograms

Figure 10. (a) The vertical components of the velocity seismograms considered in this study for *P* waveform analysis, corrected for the instrumental response. On the right is reported the station name. For each seismogram, the amplitude velocity has been normalized to its maximum. (b) Some of the vertical recordings discarded in this study. The secondary arrivals coming during the first period of *P* motion prevent us from estimating the *P* pulse width. (c) The selection of the *P* pulse width used in this study. The pulse width has been estimated both on the vertical component of each velocity seismogram and on the corresponding integrated displacement trace. The vertical bars on each seismogram pick, respectively, the onset of the *P* phase (T_1) and the time corresponding to the first period of the motion (T_2) (see also the text).
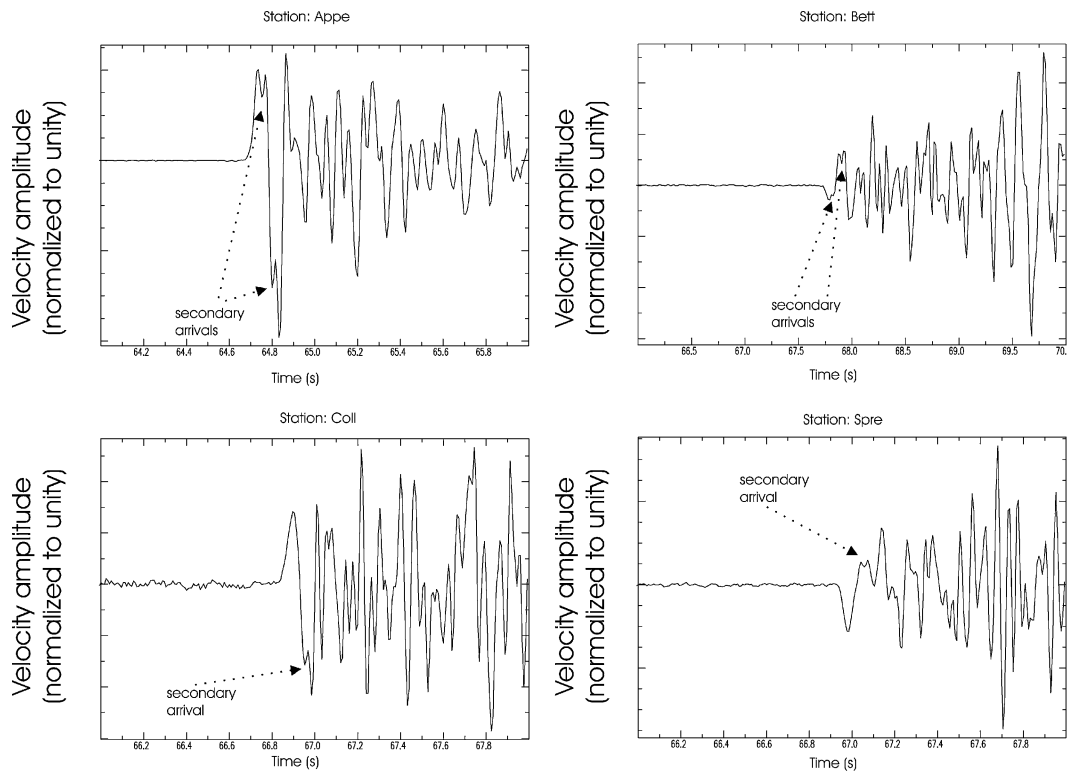
Figure 10. (*Continued.*)

it follows that in the time window $T_{01}-T_{02}$ as marked in Fig. 12, there may be a residual slight rotational component of the motion, probably caused by an *S–P* phase generated around the recording site. The pulse width as estimated from T_{01} and T_{02} is slightly higher (0.244 s) than the same as measured from T_1 and T_2 (0.219 s). The difference is around 10 per cent.

In order to estimate the uncertainties on *S* pulse widths we stress that, in the absence of secondary arrivals, by rotating the two horizontal components of a given angle, the *S* pulse width should remain stable. The variation of *S* pulse width on varying the angle of rotation is then caused by the interference of the *S* phase with these noisy components, since the latter are not generally in phase and do not have the same duration and amplitude as the *S* waves. Then, a minimum and a maximum *S* pulse width can be measured by rotating the two components and the pulse width uncertainty can be estimated to be equal to the semi-difference between these two values. An example of the pulse width uncertainty estimation is given in Fig. 13. A maximum uncertainty of 15 per cent on *S* pulse widths has been inferred using this procedure.

4.2 Modelling of source parameters at fixed rupture velocity

In this section we describe the results of the inversion of source and attenuation parameter of the studied event. We assumed $V_p = 6.1 \, \mathrm{km \, s^{-1}}$, $V_s = 3.5 \, \mathrm{km \, s^{-1}}$ and $V_r/V_s = 0.9$, according to Cattaneo *et al.* (2000).

As we discussed in the previous section our pulse width is affected, to different extents, of a given uncertainty, mainly caused by noise. In order to evaluate how the uncertainties on data affect the unknown parameters we have used the method of mapping random deviations

on the data in the model parameter space (Vasco *et al.* 1995), as also previously done for synthetic data sets.

In the first inversion we have assumed that the average uncertainty on *P* pulse width is equal to 10 per cent and that on *S* pulse width is equal to 15 per cent, as detailed in the previous section. We have represented the results of 250 inversions through the joint experimental distributions, respectively, in the planes (L, Q_p), (L, Q_s) and (δ, ϕ) (Fig. 14a). These distributions indicate well-resolved values of these parameters. In particular, the best-fitting (δ, ϕ) solution as inferred by the experimental distribution in the (δ, ϕ) plane indicates that the highest probable solution is represented by $\delta = 89°$ and $\phi = 156°$. At a lower probability level a secondary maximum in the distribution (δ, ϕ) is for $\delta = 65°$ and $\phi = 0°$. However, the quality of the fitting is different for the two solutions considered, indicating that the first solution (the standard deviation of 0.014 s) represents the global minimum and the second indicates a local minimum (standard deviation 0.025 s) of the misfit function. The best-fitting model parameters are given in Table 3.

Moreover, we must account for the fact that the uncertainty on pulse width estimates can only be estimated approximately, since the exact correction on *S* waves for multipathing would require exact knowledge of the Green function of the medium traversed by the waves. So, one may suspect that, owing also to undetected multipathing, the errors on *P* and *S* pulse widths could have been underestimated, and this could result in a further ambiguity on the fault plane which needs to be estimated. To avoid these ambiguities we have carried out another inversion run, using the same above procedure based on random deviations. We have now increased the maximum error on the *P* pulse width (15 per cent) and the maximum error on the *S* pulse width (20 per cent). The obtained results (Fig. 14b) indicate that there are no significant variations in the inferred distributions of the source parameters (in particular, on dip
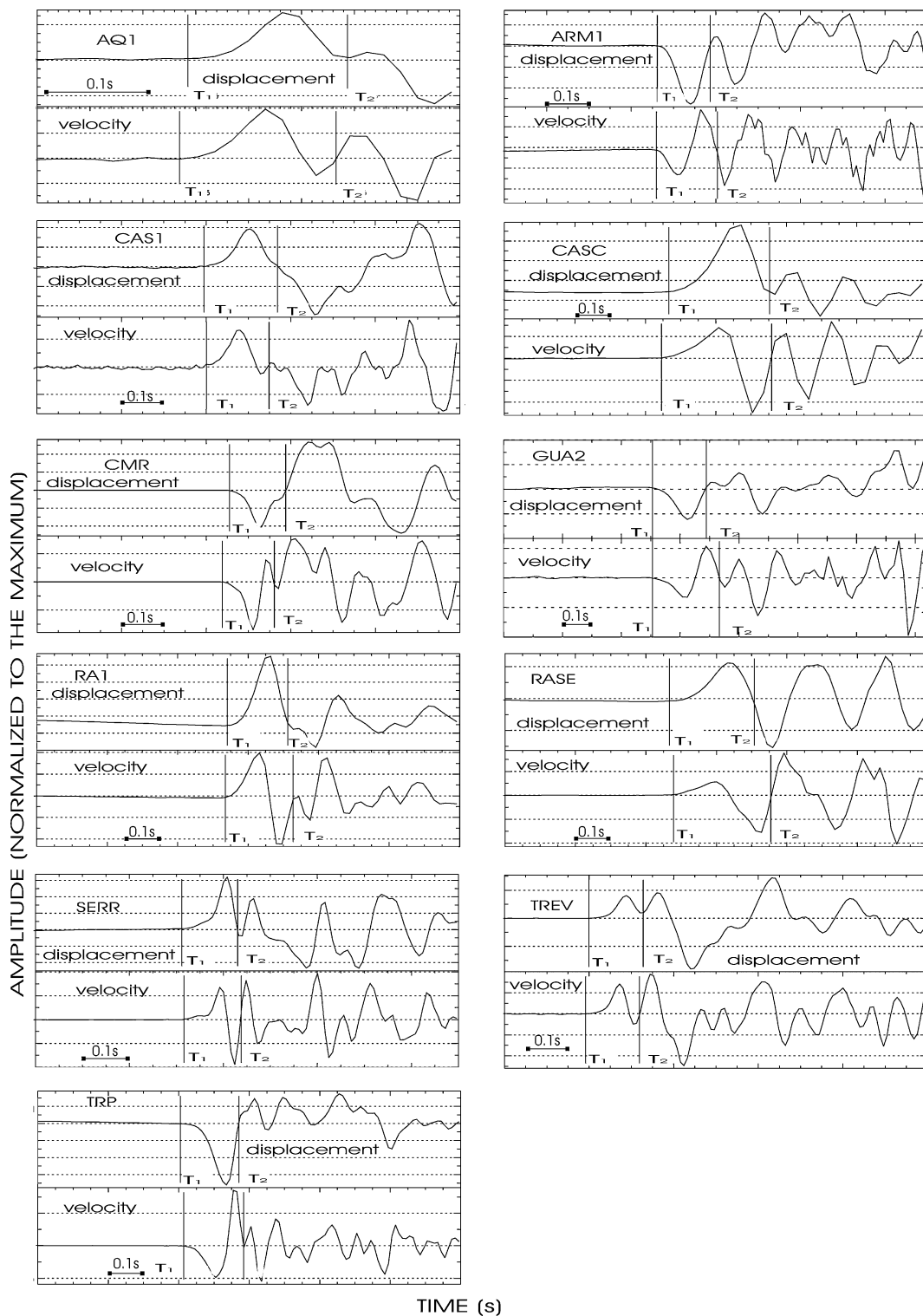
Figure 10. (*Continued.*)

and strike estimates): the best-fitting fault plane solution is always the same even if there is a slight increase in the probability of occurrence of other solutions located near the best-fitting fault orientation. Also, the (L, Q_p) and (L, Q_s) joint experimental distributions tend to be smoother around the best-fitting values previously inferred. We conclude that the model parameters stay stable, despite the increase in the assumed uncertainty on *P* and *S* pulse width estimates.

Now consider the comparison between the pulse width data and those predicted by assigning the best-fitting model parameters (Fig. 15a). It is evident that the data show pulse width variations slightly higher than those predicted by the model. An average residual of approximately 14 ms (lower than the average estimated uncertainty on data, equal to 17.5 ms) has been obtained. The differences can be generally attributed to variations of the attenuation along the
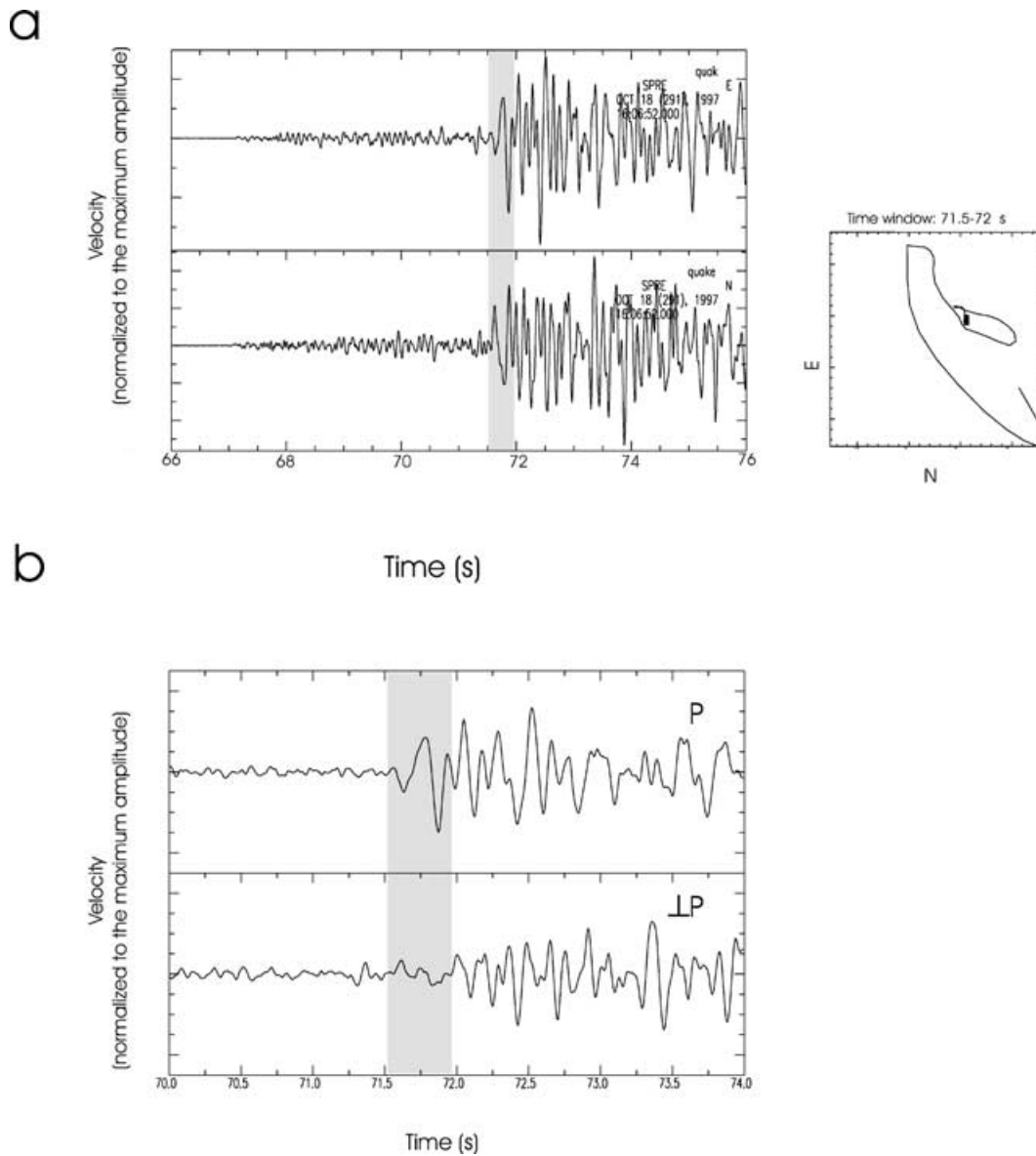
a

b

Time (s)

Time (s)

Figure 11. (a) The two horizontal (WE–SN) components of the velocity seismogram at station SPRE. On the right is plotted the (E–N) particle motion in the *S*-wave time window (the shaded zone). The east and the north axis of the particle motion plot have the same scale. The black square in the particle motion plot represents the first point of the shaded zone selected in the seismogram. (b) Seismograms showing the two components of velocity motion of (a) rotated, respectively, along the direction of predominant polarization (named R on the top seismogram) and along the direction orthogonal to R (the bottom seismogram).

Table 2. *S* pulse width estimation.

Station	Pulse width on velocity seismogram (s)	Pulse width on squared velocity seismogram (s)	Percentage difference
LAVE	0.178	0.171	4
CMR	0.204	0.198	3
SPRE	0.219	0.217	0.9
ARM1	0.187	0.185	1
RASE	0.196	0.194	1

different paths travelled by the waves (Z&D and references therein), caused by structural heterogeneities or by Q variations localized around the recording site: at stations where the theoretical pulse width is greater than the observed value, the true quality factor along the path is lower than the average inferred Q and conversely. So, we can use these residuals to estimate the difference ΔQ_{path} between the true Q (Q_{true}), along each path, and the average inferred (Q_{ave}), by simply assuming the following relationship:

$$\Delta T_{\text{true}} = \Delta T_0 + C \frac{T}{Q_{\text{true}}}, \tag{8}$$

where $Q_{\text{true}} = Q_{\text{ave}} + \Delta Q$. The obtained Q_{true} are given in Fig. 15(b).

4.3 Inferences on rupture velocity

Inferences on rupture velocity are usually difficult to obtain since this parameter is strongly correlated with the source radius both in the time and in the frequency domain. To overcome this problem some authors (see Deichmann 1997, and references therein) proposed to study the *P*-to-*S* pulse width ratios that, for the elastic case (eq. 1), are independent on the source radius:
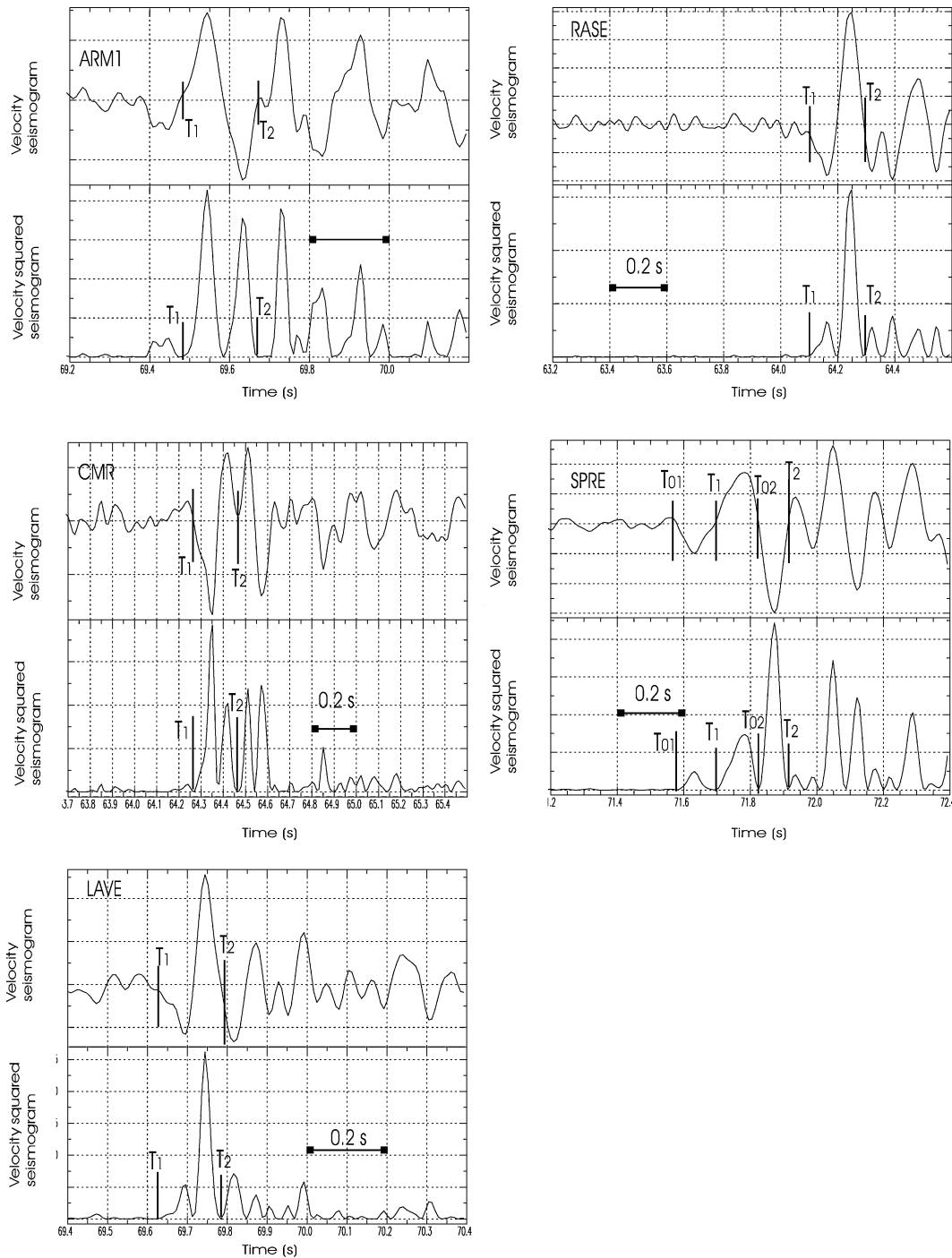
Figure 12. The *S* pulse widths selected in this study. The vertical bars on each seismogram pick, respectively, the time onset T_1 of the R component of *S* phase and the time T_2 corresponding to the first period of the motion. Each velocity seismogram (at the top of each couple of seismograms) has been compared with the corresponding squared velocity seismogram (at the bottom of each couple of seismograms) (see the text). The velocity seismograms have been normalized to the maximum amplitude.

$$\frac{\Delta T_{0,p}}{\Delta T_{0,s}} = \frac{1 + (V_p/V_r)\sin\theta}{1 + (V_s/V_r)\sin\theta}. \tag{9}$$

However, for an anelastic medium, owing to the dependence of C_p and C_s on V_r given by eqs (5) and (6), eq. (9) is no longer valid, in that the *P*-to-*S* pulse width ratio depends on the C_p and C_s values.

In this case we can hope to obtain information on the rupture velocity only by comparing the results of inversions at different rupture velocities.

Using eq. (9) we carried out the inversions of pulse width data for different V_r/V_s ratio. The results (Table 3) indicate that the quality of the different inversions is almost the same. So, we can conclude
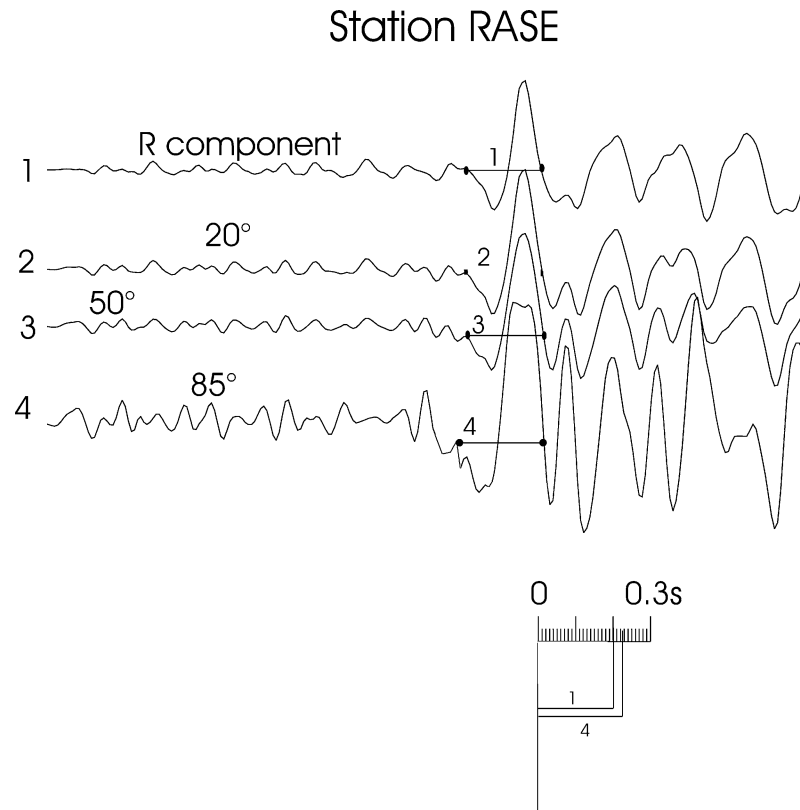
Station RASE

Figure 13. Example of estimation of *S* pulse width uncertainties at station RASE. By rotating the horizontal components in the range 0°—90° the time difference between the onset of the *S* phase and the time corresponding to the first period of motion vary from a minimum (segment 1) and a maximum (segment 4). The semi-difference between the length of these two segments is used as estimate of the uncertainty associated with the *S* pulse width.

Table 3. Model parameter estimates for the studied event. The associated uncertainties are obtained by the statistical analysis of 250 inversion on noisy data sets (see the text).

V_r/V_s	L (m)	L/V_r (ms)	Dip range (deg)	Strike (deg)	Q_p	Q_s	Average residual (ms)
0.1	45 ± 22	60	$84° \pm 10°$	$153° \pm 13°$	325 ± 23	327 ± 31	18
0.3	119 ± 18	83	$85° \pm 10°$	$152° \pm 11°$	334 ± 37	330 ± 40	16
0.5	180 ± 12	78	$88° \pm 11°$	$151° \pm 14°$	336 ± 32	315 ± 23	15
0.7	229 ± 15	56	$84° \pm 10°$	$150° \pm 12°$	329 ± 28	312 ± 22	15
0.9	268 ± 13	67	$89° \pm 9°$	$156° \pm 13°$	320 ± 20	300 ± 28	14

that the rupture velocity is not sufficiently constrained by the data. Nevertheless, the lack of resolution on V_r does not affect the resolution of the fault plane orientation. In fact, the (δ, ϕ) estimates arising from different choices of rupture velocity are practically the same. The only parameter that progressively decreases with decreasing V_r/V_s ratio is the fault radius, as a consequence of the well-known trade-off among L and V_r arising from the functional form of the non-directive source pulse width, given by $\Delta T_0 = L/V_r$.

4.4 Inversion of *P* polarities and *S* polarizations

Independent information on the fault plane orientation of the two considered events can be obtained by inverting *P* polarities and *S* polarizations of first *P* and *S* arrivals, according to the method proposed by Zollo & Bernard (1991). The *S* polarizations have been measured by averaging the time polarization values of the selected *S* waves on bandpass filtered traces (1–8 Hz). On the same considered waveforms we measured the *P* polarities and the *S* polarizations. An average uncertainty of approximately 10° on the direction of the *S* vectors has been estimated. If we indicate by $P(\delta, \phi, \lambda)$ the value of the density probability function at the point (δ, ϕ, λ), where λ is the slip direction, the cumulative probability density function (CPDF) at the point (δ, ϕ) (that is the probability density of obtaining (δ, ϕ) independently on λ) is given by the following relationship:

$$P(\delta, \phi) = \int_{-\pi}^{\pi} P(\delta, \phi, \lambda)\, d\lambda. \tag{10}$$

By analysing the CPDF in the δ–ϕ plane, shown in Fig. 16, it follows that both dip and strike are well constrained by *P* polarities and *S* polarization data; the inferred dip is slightly lower than that estimated by pulse width inversion. However, the CPDF solution lies inside the (δ, ϕ) area inferred by pulse width inversion where standard deviation is less then 1σ.

Since the inferred solution of the pulse widths indicates a near-vertical fault ($\delta = 89°$) the double solution arising from inspection of Fig. 16(b), as we discussed in the resolution study, is only an artefact of the graphical representation of the results, in that the two obtained solutions are practically the same as ($\delta = 90°$, $\phi = 156°$) and ($\delta = 90°$, $\phi = 336°$), representing the same fault.
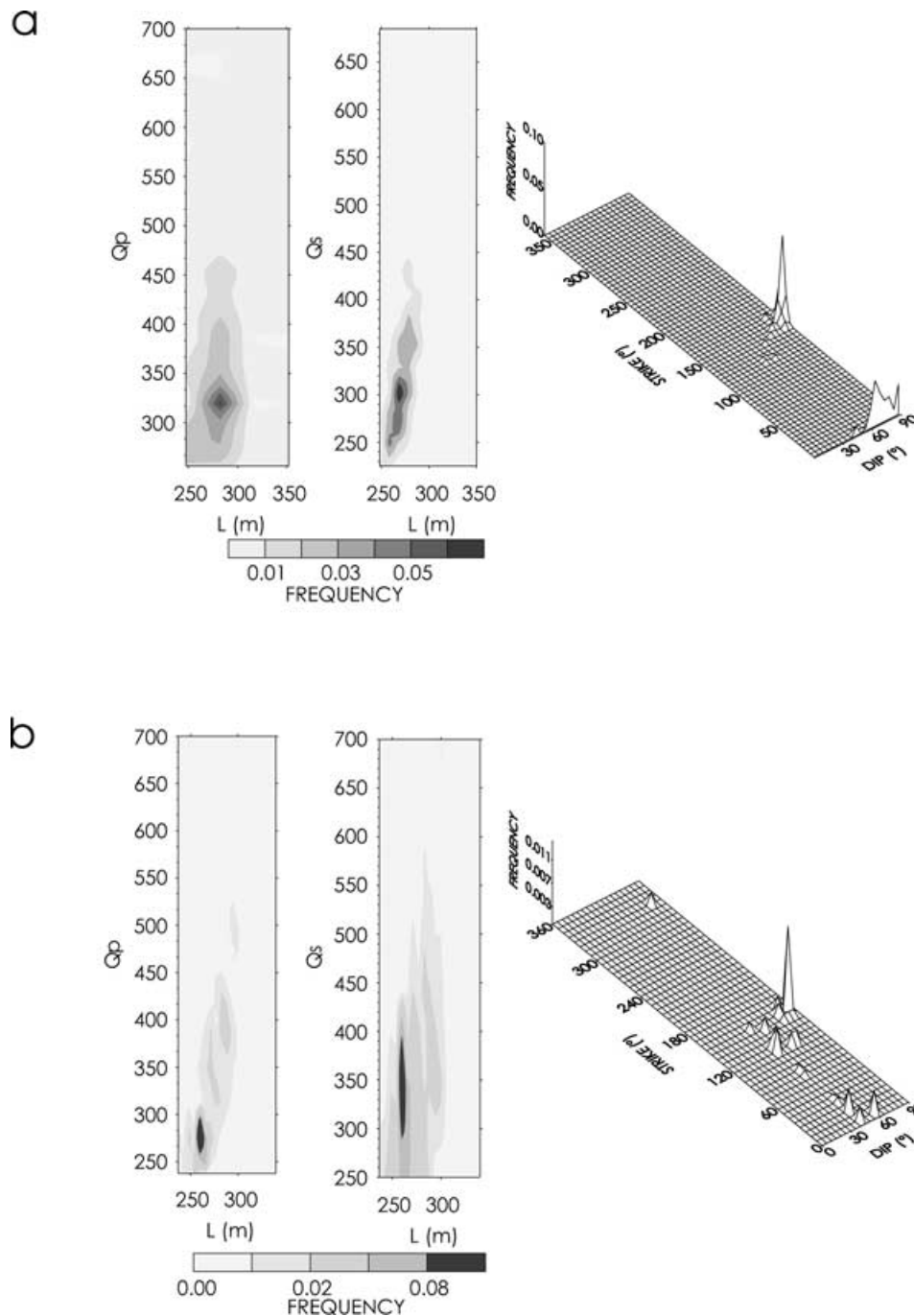
Figure 14. Results of the inversion of the data set through the random deviations approach. Plot of the frequency distribution of the retrieved solutions, in the (L, Q_p), (L, Q_s) and (δ, ϕ) planes, respectively. Case A): maximum uncertainty on *P* pulse widths equal to 10 per cent and maximum uncertainty on *S* pulse widths equal to 15 per cent. Case B): maximum uncertainty on *P* pulse widths equal to 15 per cent and maximum uncertainty on *S* pulse widths equal to 20 per cent.

5 DISCUSSION AND CONCLUSION

In this paper we have shown that *P* and *S* pulse width data of a low-magnitude earthquake can be used to obtain useful information on the fault plane orientation. The generalization of the pulse width method proposed in Z&D to the crustal range of V_p and V_s values has been carried out (eqs 4 and 5); this now allows for the applicability of the method to any area. Also, we investigated, for given V_p and

V_s the change in the slope of pulse widths versus t^* by varying V_r (eqs 6 and 7).

Our analysis was mainly focused to establish the actual resolution in fault plane orientation. It is worthwhile to recall that, in all the synthetic simulations, we never observed a trade-off between the fault radius and the quality factors of the medium; also, the quasi-ellipsoidal shape of the frequency distributions, with axes parallel to the coordinate axes, in the (L, Q_p) and (L, Q_s) planes, as inferred by
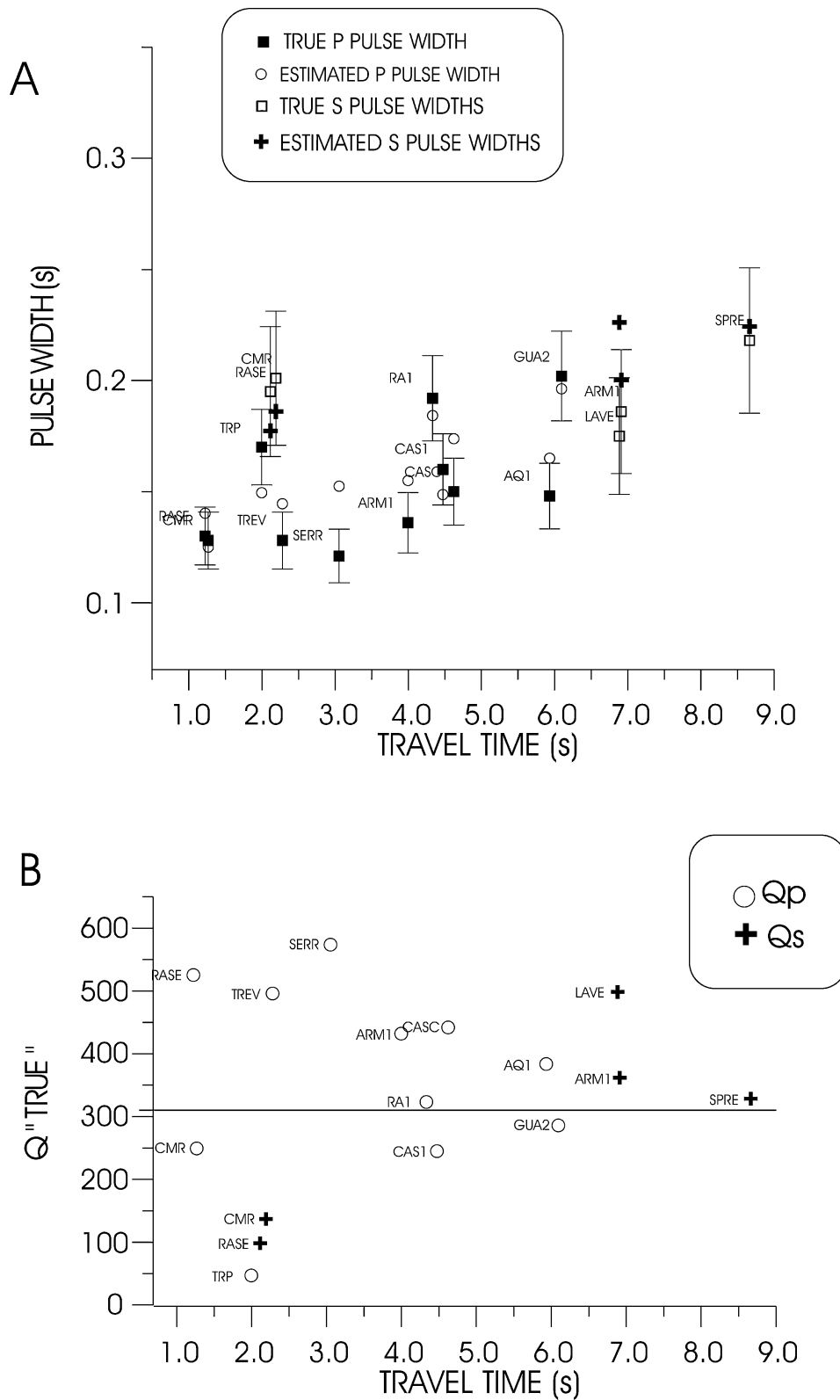
Figure 15. (a) Comparison between true and predicted pulse widths for the studied event. The *P* pulse widths have been computed by averaging the two different estimates of Table 1. The *S* pulse widths have been computed by averaging the two different estimates of Table 2. (b) Plot of Q_{true} versus traveltime. The horizontal straight line is the average *Q* used as reference.
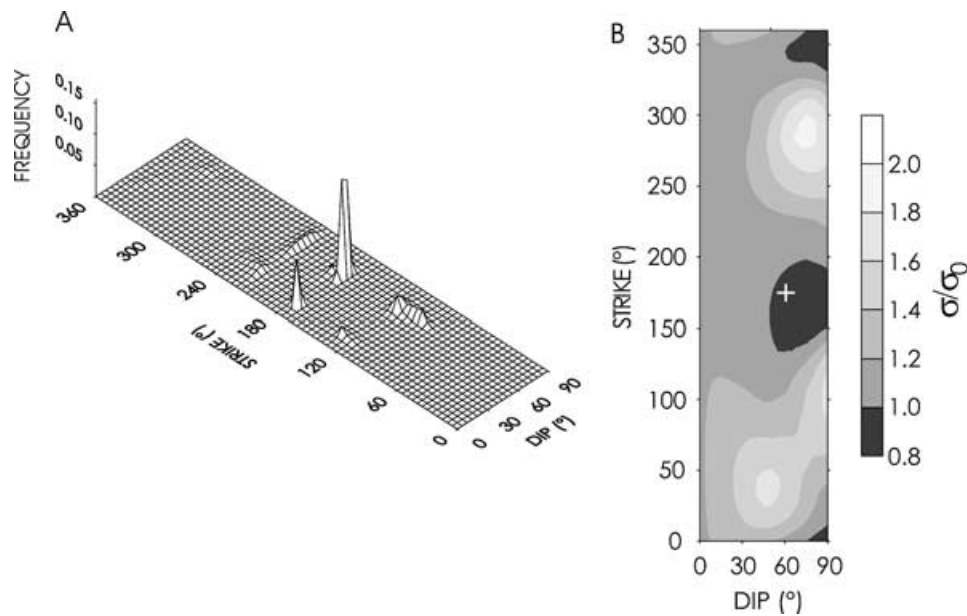
Figure 16. (a) Plot of the cumulative probability distribution function in the (δ, ϕ) plane after the inversion of *P* polarities and *S* polarizations of the studied event. (b) Plot of the $\sigma (\delta, \phi)/\sigma_0$ function in the (δ, ϕ) plane for the considered event. The white cross represents the solution as inferred by inversion of *P* polarities and *S* polarizations in (a).

random deviations analysis (Figs 14a and b) indicates the absence of correlation (Menke 1984) between L, Q_p and Q_s in the studied real case. This result arises by the use of data from different stations as also shown in other analyses (Scherbaum 1990, Z&D).

The simulations carried out allowed us to establish in what cases the fault plane is well determined by the pulse width inversion; the loss of resolution, generally related to the poor coverage of the data space, can be ascribed to the reduction of directivity effects (low variations of the take-off angles with respect to their average value). As detailed above, the parameter that better quantifies this directivity effect is the η parameter.

We applied the method to a seismic event recorded in the Umbria-Marche region. Pulse widths of both *P* and *S* waves show strong variability with distance and do not follow the linear trend expected for non-directive sources.

The results of the statistical study based on the random deviations technique indicate that the fault plane orientation remains stable, also when a higher uncertainty on *P* and *S* pulse widths is assumed. This is an important result in that it indicates that pulse width data, despite their uncertainties, contain striking information on the fault plane orientation. Since the onset of the *S* wave at station LAVE is not quite clear, we carried out another inversion, neglecting the *S* pulse width at this station. The obtained results were the same.

The misfit between true and predicted data can be used to compute the variations in the amount of inelastic attenuation along the different ray paths travelled owing to structural heterogeneities and/or localized site attenuation or amplification effects. Also, it can be easily shown that, under the assumption of a non-directive source, the Q_p and Q_s path corrections required to obtain a nil misfit are much higher, in that the variability around the best-fitting line of ΔT versus traveltime data is, in this case, ascribed only to Q variations. Therefore, the use of a directive source allows for a smoother attenuation model of the area with respect to the non-directive assumption, without invoking an *a priori* smoothing constraint to reduce roughness in the attenuation model, as is often needed in tomographic attenuation studies (e.g. Wu & Lees 1996).

Also, we accounted for the error inherent to the assumptions we made (constant rupture velocity, absence of healing phases, quasi-constant Q attenuation model). Also for this reason we tested the stability of the solution by increasing the expected uncertainty on *P* and *S* pulse widths. Always for the same reason, we tested our results versus the fault plane solution as inferred by *P* polarities and *S* polarizations inversion, obtaining comparable results.

The average Q_p and Q_s quality factors inferred from the inversion assume practically the same value, when we account for the estimated uncertainties on these parameters. Interestingly, $Q_p = Q_s$ has also been found in another study (Abercrombie 1995) where the use of borehole seismograms prevented site effects.

The estimated difference between the Q_{true} along each path and Q_{ave} are not surprising in that the ray-sampled area is characterized by relevant structural variations, being located inside a mountain chain, the central–northern Apennine; in any case, these represent the minimum Q variations we can obtain using pulse width data, as detailed above. We have inferred that Q_p and Q_s suffer a strong variation with varying distance (Fig. 15b), ranging from a minimum of approximately 50–100 to a maximum of approximately 600. Despite the different techniques used to estimate the attenuation parameters, the range of Q_s variations we inferred are practically coincident with those of Q_c (Q of *S* coda) as inferred by Del Pezzo & Zollo (1984) in part of the studied area, the Norcia town (Umbria). Moreover, even if in our study we used only an event, which prevents generalization of our attenuation estimates to the entire area, our results are in a good agreement with the conclusions reported in a recent attenuation study (Castro *et al.* 2002). The authors found that the strong spatial variability of Q estimates may depend on spatial and temporal variations of tectonic stress in the epicentral area other than on the fault structure.

Another point that needs further discussion concerns the adopted source model. One may think that the source parameters inferred in this study are strictly dependent on the assumptions inherent to the adopted source model (i.e. a circular crack that ruptures at a constant velocity). As we will try to show, the obtained results are slightly

more general and inherent to the basic assumptions of kinematics of the seismic source. First, we remark that the starting point of the developed model is represented by the functional dependence of the source pulse width ΔT_0 on the source parameters, as given by eq. (1). It is worthwhile to recall that eq. (1) is a simplified relationship that arises from the basic assumptions of the kinematics of the seismic source, in the far-field range (Fraunhofer approximation) (Aki & Richards 1980); it still remains valid if we consider an unidimensional fault model (e.g. Haskell 1964). Then, by considering the inelasticity of rocks, other than the source contribution to the pulse width, one must account for the attenuation term, given by Ct/Q, where C is dependent on the source time function, as shown in several papers (Liu 1988; de Lorenzo 1998). Based on this reasoning, one may expect that, by recalibrating eq. (2) for a rectangular fault model, a different dependence of C on V_p and V_s values at the source may be inferred. This is the focus of the discussion in that, as long as eq. (2) remains valid, the use of a different C cannot modify the retrieved fault plane orientation, but only the Q estimates. In fact, since the C/Q term controls only the slope of ΔT versus traveltime, by using a different C, a different Q will be inferred. Nevertheless, since the source pulse width term ΔT_0 does not depend on C, the use of a different C cannot affect either the intercept term (from which the fault length or the fault radius can be inferred) or the dispersion of data around the best-fitting straight line due to the directivity effects (from which δ and ϕ are estimated).

Owing to the simplicity of the approach, we think that the proposed method may also be very useful in a preliminary stage of an EGF source study aimed at inferring the slip distribution of a greater earthquake (e.g. Fletcher & Spudich 1998). It is, in fact, well known that the low-magnitude event one must select for the deconvolution should be representative only of instrument, path and site effects. The results of our study indicate that, at the scale of a local array, depending on data uncertainties, the directivity of the source may also be revealed for earthquakes of very low magnitude; for instance, the example shown in Fig. 6(b) indicates that only for $L < 10$ m is the directivity quite lost. This clearly implies that, in this case, the low-magnitude event considered for deconvolution in the EGF should have a fault length of less than 10 m to avoid distortion of the inferred directivity function.

Results of this study seem to indicate that pulse width data probably contain a number of pieces of information on the rupture properties higher than those we used in a simplified model (constant rupture velocity and abrupt stopping of rupture). In fact, the higher variability of pulse width data with respect to the predicted ones could also indicate, other than variability of the site response, source effects that cannot be reproduced with the actual model. So we think that further studies, aimed at evaluating the role of a variable rupture velocity (e.g. Sato 1994) and/or the healing phases (e.g. Fukuyama & Madariaga 1998) on the shape and duration of signals generated by a microearthquake, could help to better explain the variability of pulse width data with varying distance.

Finally, the (δ, ϕ) estimates for the two events are quite stable with varying rupture velocity and this should indicate the absence of a correlation between the fault plane orientation and the rupture velocity. This is very important as V_r is the parameter less constrained by the inversion of the pulse width data.

ACKNOWLEDGMENTS

REFERENCES

Abercrombie, R.E., 1995. Earthquake source scaling relationship from −1 to 5 M_L using seismograms recorded at 2.5-km depth, *J. geophys. Res.,* **100,** 24 015–24 036.

Abercrombie, R.E., Bannister, S., Pancha, A., Webb, T.E. & Mori, J.J., 2001. Determination of fault planes in a complex aftershock sequence using two-dimensional slip inversion, *Geophys. J. Int.,* **146,** 134–142

Aki, K. & Richards, P.G., 1980. *Quantitative Seismology: Theory and Methods,* Vol. I and II, p. 932, Freeman, San Francisco.

Anderson, J.G. & Hough, S.E., 1984. A model for the shape of the Fourier amplitude spectrum at high frequencies, *Bull. seism. Soc. Am.,* **74,** 1969–1993.

Azimi, S.A., Kalinin A.V., Kalinin V.V. & Pivovarov, B.L., 1968. Impulse and transient characteristic of media with linear and quadratic absorption laws, *Izvest., Phys. Solid Earth,* **2,** 88–93.

Bernard, P. & Zollo, A., 1989. Inversion of near-source S polarization for parameters of double-couple point sources, *Bull. seism. Soc. Am.,* **79,** 1779–1809.

Blair, D.P. & Spathis, A.T., 1982. Attenuation of explosion generated pulse in rock masses, *J. geophys. Res.,* **87,** 3885–3892.

Boatwright, J., 1980. A spectral theory for circular seismic sources: simple estimates of source dimension, dynamic stress drop and radiated seismic energy, *Bull. seism. Soc. Am.,* **70,** 1–28.

Boatwright, J., 1984. The effect of rupture complexity in estimate of source size, *J. geophys. Res.,* **89,** 1132–1146.

Brune, J.N., 1970. Tectonic stress and the spectra of seismic shear waves from earthquakes, *J. geophys. Res.,* **75,** 4997–5009.

Castro, R.R., Monachesi, G., Trojani, L., Mucciarelli, M. & Frapiccini, M., 2002. An attenuation study using earthquakes from the 1997 Umbria-Marche sequence, *J. Seismol.,* **6,** 43–59.

Cattaneo, M. *et al.*, 2000. The 1997 Umbria-Marche (Italy) earthquake sequence: analysis of data recorded by the local and temporary network, *J. Seismol.,* **4,** 401–414.

Courboulex, F., Virieux, J., Deschamps, A., Gibert, D. & Zollo, A., 1996. Source investigation of a small event using empirical Green functions and simulated annealing, *Geophys. J. Int.,* **125,** 768–780

Courboulex, F., Deichmann, N. & Gariel, J.-C., 1999. Rupture complexity of a moderate intraplate earthquake in the Alps: the 1996 M5 Rpagny-Annecy earthquake, **139,** 152–160.

Crampin, S., 1985. Evaluation of anisotropy by shear wave splitting, *Geophysics,* **50,** 159–170.

de Lorenzo, S., 1998. A model to study the bias on Q estimates obtained by applying the rise time method to earthquake data, in *Q of the Earth, Global, Regional and Laboratory Studies,* Vol. 153, pp. 419–438, eds Mitchell, B.J. & Romanowicz, B., Pure and Appl. Geophys.

Del Pezzo, E. & Zollo, A., 1984. Attenuation of coda waves and turbidity coefficient in Central Italy, *Bull. seism. Soc. Am.,* **74,** 2665–2679.

Deichmann, N., 1997. Far field pulse shapes from circular sources with variable rupture velocities, *Bull. seism. Soc. Am.,* **87,** 1288–1296.

Deichmann, N., 1999. Empirical Green's function: a comparison between pulse width measurements and deconvolution by spectral division, *Bull. seism. Soc. Am.,* **89,** 178–189.

Fletcher, J.B. & Spudich, P., 1998. Rupture characteristics of the three M 4.7 (1992–1994) Parkfield earthquakes, *J. geophys. Res.,* **103,** 835–854.

Fukuyama, E. & Madariaga, R., 1998. Rupture dynamics of a planar fault in a 3D elastic medium: rate-and slip-weakening friction, *Bull. seism. Soc. Am.,* **88,** 1–17.

Gladwin, M.T. & Stacey, F.D., 1974. Anelastic degradation of acoustic pulses in rock, *Phys. Earth planet. Inter.,* **8,** 332–336.

Govoni, A., Spallarossa, D., Augliera, P. & Trojani, L., 1999. *The 1997 Umbria-Marche Earthquake Sequence: the Combined Data Set*

of the GNDT/SSN Temporary and the RESIL/RSM Permanent Seismic Networks, (Oct. 18–Nov. 3, 1997), Project GNDT-CNR: PROGETTO ESECUTIVO 1998, 6a1, "Struttura e sorgente della sequenza" (coordinator: M. Cattaneo) (on electronic CD-ROM support).

Hartzell, S.H., 1978. Earthquake aftershocks as Green's functions, *Geophys. Res. Lett.,* **5,** 1–4.

Haskell, N., 1964. Total energy and energy spectral density of elastic wave radiation from propagating faults, *Bull. seism. Soc. Am.,* **54,** 1811–1842.

Hough, S.E., Lees, J.M. & Monastero, F., 1999. Attenuation and source properties at the Coso Geothermal Area, California, *Bull. seism. Soc. Am.,* **89,** 1606–1619.

Huang, W.C. *et al.*, 2000. Seismic polarization anisotropy beneath the Central Tibetan Plateau, *J. geophys. Res.,* **105,** 27 979–27 989.

Ichinose, G.A., Smith, K.D. & Anderson, J.G., 1997. Source parameters of the 15 November 1995 Border Town, Nevada, earthquake sequence, *Bull. seism. Soc. Am.,* **87,** 652–667.

Kjartansson, E., 1979. Constant Q-wave propagation and attenuation, *J. geophys. Res.,* **84,** 4737–4748.

Liu, H.-P., 1988. Effect of source spectrum on seismic attenuation measurements using the pulse broadening method, *Geophysics,* **53,** 1520–1526.

Liu, H.-P., Warrick, R.E., Westerlund, J.B. & Kayen, E., 1994. *In situ* measurement of seismic shear-wave absorption in the San Francisco Holocene Bay Mud by the pulse-broadening method, *Bull. seism. Soc. Am.,* **84,** 62–75.

Madariaga, R., 1976. Dynamics of an expanding circular fault, *Bull. seism. Soc. Am.,* **66,** 639–666.

Menke, W., 1984. *Gephysical Data Analysis: Discrete Inverse Theory,* Academic, New York.

Mori, J., 1996. Rupture directivity and slip distribution of the M 4.3 foreshock to the 1992 Joshua Tree Earthquake, Southern California, *Bull. seism. Soc. Am.,* **86,** 805–810.

Mori, J. & Hartzell, S., 1990. Source inversion of the 1988 Upland, California, earthquake. Determination of a fault plane for a small event, *Bull. seism. Soc. Am.,* **80,** 507–518.

Nelder, J.A. & Mead, R., 1965. A simplex method for function minimization, *Comp. J.,* **7,** 308–313.

Sato, T., 1994. Seismic radiation from circular cracks growing at variable rupture velocity, *Bull. seism. Soc. Am.,* **84,** 1199–1215.

Sato, T. & Hirasawa, T., 1973. Body wave spectra from propagating shear cracks, *J. Phys. Earth.,* **21,** 415–432.

Scherbaum, F., 1990. Combined inversion for the three-dimensional Q structure and source parameters using microearthquake spectra, *J. geophys. Res.,* **95,** 12 423–12 438.

Wu, H. & Lees, M., 1996. Attenuation structure of Coso geothermal area, California, from wave pulse widths, *Bull. seism. Soc. Am.,* **86,** 1574–1590.

Vasco, D.W., Johnson, L.R. & Pulliam, J., 1995. Lateral variation in mantle structure and discontinuities determined from *P*, *PP*, *S*, *SS* and *SS–SdS* travel time residuals, *J. geophys. Res.,* **100,** 24 037–24 060.

Zollo, A. & Bernard, P., 1989. *S*-wave polarization inversion of the 15 October 1979, 23:19 Imperial Valley aftershock: evidence for anisotropy and a simple source mechanism, *Geophys. Res. Lett.,* **16,** 1047–1050.

Zollo, A. & Bernard, P., 1991. Fault mechanisms from near source data: joint inversion of *S* polarizations and *P* polarities, *Geophys. J. Int.,* **104,** 441–451.

Zollo, A. & de Lorenzo, S., 2001. Source parameters and three-dimensional attenuation structure from the inversion of microearthquake pulse width data: method and synthetic tests, *J. geophys. Res.,* **106,** 16 287–16 306.

Zollo, A., Capuano, P. & Singh, S.K., 1995. Use of small earthquake record to determine the source time function of larger earthquakes: an alternative method and an application, *Bull. seism. Soc. Am.,* **85,** 1249–1256.